

# The First Terrestrial Electron Beam Observed by The Atmosphere-Space Interactions Monitor

D. Sarria<sup>1</sup>, P. Kochkin<sup>1</sup>, N. Østgaard<sup>1</sup>, N. Lehtinen<sup>1</sup>, A. Mezentsev<sup>1</sup>, M.  
Marisaldi<sup>1</sup>, B.E. Carlson<sup>1,2</sup>, C. Maiorana<sup>1</sup>, K. Albrechtsen<sup>1</sup>, T. Neubert<sup>3</sup>, V.  
Reglero<sup>4</sup>, K. Ullaland<sup>1</sup>, S. Yang<sup>1</sup>, G. Genov<sup>1</sup>, B. H. Qureshi<sup>1</sup>, C.  
Budtz-Jørgensen<sup>3</sup>, I. Kuvvetli<sup>3</sup>, F. Christiansen<sup>3</sup>, O. Chanrion<sup>3</sup>, M.  
Heumesser<sup>3</sup>, K. Dimitriadou<sup>3</sup>, J. Navarro-González<sup>4</sup>, P. Connell<sup>4</sup>, C. Eyles<sup>4</sup>

<sup>1</sup>Birkeland Centre for Space Science, University of Bergen, Bergen, Norway

<sup>2</sup>Carthage College, Kenosha, Wisconsin, United States

<sup>3</sup>National Space Institute, Technical University of Denmark, Lyngby, Denmark

<sup>4</sup>University of Valencia, Valencia, Spain

## Key Points:

- Flying over an area with no nearby lightning activity, the ASIM-MXGS instrument detected a four ms long event with a soft spectrum.
- Observations coupled with simulations suggest that more than 90% of the counts come from a TEB, and the rest from the associated TGF.
- A source TGF with a broad angular distribution and  $10^{17.2}$  to  $10^{18.9}$  photons can explain the observation.

---

Corresponding author: D. Sarria, david.sarria@uib.no

-1-

This article has been accepted for publication and undergone full peer review but has not been through the copyediting, typesetting, pagination and proofreading process which may lead to differences between this version and the Version of Record. Please cite this article as doi: 10.1029/2019JA027071

**Abstract**

We report the first Terrestrial Electron Beam (TEB) detected by the Atmosphere-Space Interactions Monitor (ASIM). It happened on September 16th, 2018. The ASIM Modular X and Gamma-ray Sensor (MXGS) recorded a two millisecond long event, with a softer spectrum than typically recorded for Terrestrial Gamma-ray Flashes (TGF). The lightning discharge associated to this event was found in the World-Wide Lightning Location Network (WWLLN) data, close to the northern footpoint of the magnetic field line that intercepts the International Space Station (ISS) location. Imaging from a GOES-R geostationary satellite shows that the source TGF was produced close to an overshooting top of a thunderstorm. Monte-Carlo simulations were performed to reproduce the observed lightcurve and energy spectrum. The event can be explained by the secondary electrons and positrons produced by the TGF (i.e. the TEB), even if about 3.5% to 10% of the detected counts may be due to direct TGF photons. A source TGF with a Gaussian angular distribution with standard deviation between  $20.6^\circ$  and  $29.8^\circ$  was found to reproduce the measurement. Assuming an isotropic angular distribution within a cone, compatible half angles are between  $30.6^\circ$  and  $41.9^\circ$ , in agreement with previous studies. The number of required photons for the source TGF could be estimated for various assumption of the source (altitude of production, angular distribution), and is estimated between  $10^{17.2}$  and  $10^{18.9}$  photons, i.e. compatible with the current consensus.

**Plain Language Summary**

Terrestrial Gamma-Ray Flashes (TGFs) are the highest energy natural particle acceleration phenomena occurring on Earth. They are burst of energetic photons associated with thunderstorms, and have a poorly understood production mechanism. When interacting with the atmosphere, TGFs produce secondary electrons and positrons of high energy. A fraction of them can reach Space, and forms a beam under the effect of Earth's magnetic field, so called Terrestrial Electron Beam (TEB). They can be detected over geographical location with no lightning activity. In the past, most of the TEBs have been detected by the Fermi space telescope and the Compton Gamma-ray Observatory. In this article, we report the first detection of a TEB by the Atmosphere-Space Interactions Monitor (ASIM), docked on the International Space Station since April 2018. During this event, no lightning activity was detected below the instrument. The TEB's source lightning was actually found to be located 650 kilometers away from detector, very close to

51 an overshooting top of a thundercloud. The comparison of the observation with simu-  
52 lated data made it possible to constrain the geometry of the parent TGF. Our results  
53 point towards a relatively wide angular distribution and an intensity of  $10^{17.2}$  to  $10^{18.9}$   
54 photons, in agreement with previous studies.

## 55 1 Introduction

56 Terrestrial Gamma-ray Flashes (TGFs) are short ( $< 2$  ms) bursts of high energy  
57 ( $< 30$ - $40$  MeV) photons, produced during thunderstorms, between 10 and 15 km alti-  
58 tude, for events detectable from space. A review of the science of TGFs is presented by  
59 Dwyer et al. (2012). TGFs were first detected using the BATSE experiment on-board  
60 the NASA's CGRO spacecraft (Fishman et al., 1994). Later, TGFs were recorded from  
61 space by RHESSI (Smith et al., 2005), AGILE (MCAL instrument) (Marisaldi et al., 2014),  
62 the Fermi space telescope (GBM instrument) (Briggs et al., 2010; Roberts et al., 2018),  
63 BeppoSAX (Ursi et al., 2017) and the Atmosphere-Space Interactions Monitor (ASIM)  
64 (Neubert, Østgaard, Reglero, Blanc, et al., 2019). ASIM is the only one specifically de-  
65 signed to detect TGFs from space, using the Modular X- and Gamma-ray Sensor (MXGS)  
66 (Østgaard et al., 2019). ASIM was successfully launched and docked to the International  
67 Space Station in April 2018, and started science operations in June 2018. The first re-  
68 sults from ASIM are presented by Neubert, Østgaard, Reglero, Chanrion, et al. (2019);  
69 Østgaard et al. (2019), in addition to this article.

70 TGFs deposit a large amount of energy in the atmosphere, as a large fraction (typ-  
71 ically  $> 97\%$ ) of the initial bremsstrahlung photons is absorbed before reaching space.  
72 By colliding with the atmosphere, the photons produce a large quantity of electrons (through  
73 Compton scattering and pair production) and positrons (pair production), but only a  
74 small fraction is able to escape the atmosphere. Most of the escaping electrons are pro-  
75 duced above  $\approx 40$  km altitude (Sarria et al., 2015). Once they have escaped, the electrons  
76 and positrons are then bound to Earth's magnetic field lines and can travel large dis-  
77 tances inside the magnetosphere (Dwyer et al., 2008; Cohen et al., 2010; Briggs et al.,  
78 2011). This phenomenon is called a Terrestrial Electron Beam (TEB). The TGF respon-  
79 sible for the TEB will be referred as the "source TGF" in the rest of this article. TEBs  
80 were first reported from measurements of the BATSE/CGRO spacecraft (Dwyer et al.,  
81 2008). Later, they were detected by the Fermi space telescope (Briggs et al., 2011), one  
82 event was found in the BeppoSAX satellite data archive (Ursi et al., 2017), and RHESSI

83 also likely detected such an event (see Smith et al. (2006); and Gjesteland (2012), Fig-  
84 ure 4.6). The Fermi space telescope could also detect an event identified as both a TGF  
85 and a TEB (Stanbro et al., 2019). The duration of TEBs are several times longer than  
86 TGFs. This is because the electrons/positrons have a wide range of pitch angles (with  
87 respect to the local magnetic field direction) when they are produced and/or escape the  
88 atmosphere, which leads to a temporal dispersion after propagating several thousand of  
89 kilometers along Earth's magnetic field lines. This phenomenon is illustrated in figure  
90 1. For more information about the pitch angle distribution of TEB's electrons, see Sarria  
91 et al. (2016). A TEB typically contains 8% to 15% of positrons. All TGFs directed to  
92 space produce a TEB, but they are more difficult to detect than TGF. This is because  
93 a TGF can be detected by satellites located within a radius of about 800 km around its  
94 source, whereas TEBs extend only over a few tens of kilometers around the two point  
95 where the magnetic field line reaches the altitude of the satellite (in some cases, the apex  
96 of the magnetic field line is lower than the ISS altitude). For example, the first Fermi-  
97 GBM TGF catalog presents only 30 TEB candidates among the total of 4135 listed TGF  
98 events (Roberts et al., 2018).

99 In this article we report the first TEB event detected by ASIM, using the MXGS  
100 instrument. Although the MXGS primary objective is to detect TGFs, a long trigger win-  
101 dow (25 milliseconds) was implemented to detect longer events like TEBs. In section 2,  
102 we present the ASIM-MXGS instrument and discuss its ability to detect TEBs. In sec-  
103 tion 3, we present the event detected on September 16th, 2018. In section 4, we use Monte-  
104 Carlo simulation in order to reproduce the event and to constrain its beaming and its  
105 source content. We conclude in section 5.

## 106 **2 Instruments and data**

107 The Atmosphere-Space Interactions Monitor (ASIM) (Neubert, Østgaard, Reglero,  
108 Blanc, et al., 2019) consists of two main instruments : MXGS (Modular X- and Gamma-  
109 ray detector) for hard radiation observations and MMIA (Modular Multi-spectral Imag-  
110 ing Array) for optical observations (Chanrion et al., 2019). The MXGS instrument con-  
111 sists of a Low Energy Detector (LED) and a High Energy Detector (HED). Østgaard et  
112 al. (2019) described the instrument in details. The HED is based on twelve bismuth ger-  
113 manium oxide (BGO) scintillator crystal bars of  $15 \times 5 \times 3.2 \text{ cm}^3$  interfaced to Photo-  
114 multiplier tubes, and is sensitive to energies of  $\sim 300 \text{ keV}$  to  $\sim 40 \text{ MeV}$ . It has a total ge-

115 ometrical area of  $900 \text{ cm}^2$ . The LED consists of an array of cadmium-zinc-telluride (CZT)  
116 detector crystals with a total of 16384 pixels, and geometrical area of  $1024 \text{ cm}^2$ . It op-  
117 erates in the energy range of  $\sim 70 \text{ keV}$  to  $\sim 400 \text{ keV}$ . The LED only operates during nigh-  
118 time, and the event reported in this article happened during daytime. MXGS uses 4 trig-  
119 ger time windows:  $300 \mu\text{s}$ ,  $1 \text{ ms}$ ,  $3 \text{ ms}$  and  $25 \text{ ms}$ , this last being specifically implemented  
120 to target TEBs. For both detectors, if the recorded number of count exceeds a given thresh-  
121 old within one of these time windows, the MXGS instrument triggers, and saves high res-  
122 olution data of every single recorded count inside a time frame of approximately  $\pm 1 \text{ sec}$ -  
123 ond around the trigger time.

124 ASIM is mounted to the Columbus module on the International Space Station (ISS)  
125 since April 2018. The ISS has been designed to always show the same side to the Earth,  
126 meaning that MXGS is always pointing towards the nadir. Let  $\theta$  be the angle, measured  
127 from the ISS, between the nadir and the location of a TGF. All TGF events are expected  
128 to come with  $\theta < 70^\circ$ . TEB's electrons and positrons are bounded to Earth's magnetic  
129 field lines and perform helical motion around it and therefore can hit the space station  
130 from any angle of incidence.

131 In order to simulate the response of MXGS to TGF and TEB, we developed a com-  
132 plete mass model of the instrument (Østgaard et al., 2019), based on the Geant4 toolkit  
133 (Agostinelli et al., 2003; Allison et al., 2006, 2016). It includes all relevant elements around  
134 the instrument, in particular the HED, LED, coded mask, shielding and electronics, MMIA,  
135 mounting platform, the other mounted instruments, and the Columbus module. By Monte-  
136 Carlo simulations we estimated that the effective area of the HED for a typical TEB is  
137 about  $150 \text{ cm}^2$ , which is about 25% of the one for a typical TGF. In this case the effec-  
138 tive area is calculated as the geometrical area ( $\approx 900 \text{ cm}^2$  for HED and  $\approx 1024 \text{ cm}^2$  for  
139 LED) multiplied by the probability of an incident TEB electron to deposit more than  
140  $400 \text{ keV}$  into at least one BGO crystal. This energy deposition can be direct (electrons/positrons  
141 hitting the crystal) or indirect. In the indirect case, electrons/positrons emit bremsstrahlung  
142 photons by interaction with the surrounding material, that hit at least one BGO crys-  
143 tal. Each positron can also be affected by the annihilation process that takes place at  
144 the end of each track, when the kinetic energy goes down to zero. For HED, the indi-  
145 rect processes are mostly involved during TEB events, because of the shielding around  
146 the crystals stops most of the electrons/positrons. The effective area is a function of the  
147 energy of the electrons and positrons, and the value given previously is an average over

148 a typical TEB spectrum. In addition to HED, we also estimated that the effective area  
149 of the LED detector for TEB detection is about 280 cm<sup>2</sup>. It is significantly larger than  
150 for HED because direct electron hits are much more likely. It implies that, during a TEB  
151 event, the LED could detect twice more particles than the HED. This prediction should  
152 be testable with future events, since the LED was not operating for the event reported  
153 here.

### 154 3 Observation

155 ASIM-MXGS recorded an unusually long event on September 16th, 2018, at 13:14:44.733601  
156 (UTC). The event was strong enough to have been triggered by the 3 ms window. The  
157 recorded lightcurve is presented in figure 2. The event consists of a pulse of more than  
158 2 ms duration. Figure 3.a. shows the geometry of the event on a map. Table 1 gives a  
159 summary of the coordinates and times of the interesting points.

160 The data from World Wide Lightning Location Network (WWLLN) was also used  
161 for this analysis. It provides lightning timing and location by the use of a network of VLF  
162 sensors positioned on the ground around the globe (Hutchins et al., 2012). According  
163 to WWLLN, there was no lightning activity below the ISS within a reasonable time win-  
164 dow (few minutes) and distance (< 600 km). We could estimate the position of the mag-  
165 netic field line footpoint at 45 km altitude (approximately the altitude where most of  
166 the electrons that have a chance to escape the atmosphere are produced) in the north-  
167 ern hemisphere (see Table 1). This position was obtained from the model presented in  
168 Emmert et al. (2010), based on IGRF-12 (Thébault et al., 2015). These geographic co-  
169 ordinates were also confirmed by the two other codes, implementing the IGRF-12 model  
170 and a Runge-Kutta stepper to propagate the electrons/positrons along Earth's magnetic  
171 field (MC-PEPTITA and Geant4-based) that will be presented in section 4. Four WWLLN  
172 events were found around this location, within a time frame of less than 140 ms. Two  
173 of them are within 6 ms, well within the MXGS absolute timing uncertainty of about  
174 20 ms. Since these two events happened within 0.1 ms and are close in location, they  
175 probably belong to the same flash. The coordinates of the events are given in Table 1,  
176 as events number 3 and 4. They are respectively 13.79 km and 12.69 km away from the  
177 northern magnetic field line footpoint at 45 km altitude, knowing that the WWLLN has  
178 a generic positioning uncertainty of  $\pm 15$  km. The probability of having a WWLLN event  
179 in such a narrow time window and position by random chance is extremely low. There-

180 fore these two points are likely close to the location of a lightning flash associated with  
181 the TGF that generated the TEB that was recorded by MXGS. In addition, simulated  
182 data, presented in section 4, also indicate that the time between the TGF production  
183 and the first electron reaching the detector is about 2.3 ms, which is close to travel time  
184 at the speed of light along the magnetic field line.

185 As it has been observed previously (see e.g. Briggs et al. (2011); Ursi et al. (2017)),  
186 a TEB could, in principle, come from a source TGF located at the magnetic footprint  
187 of the opposite hemisphere. For this event, it is located at  $\lambda = -29.920^\circ$  (latitude),  $\phi =$   
188  $-101.044^\circ$  (longitude). However, we could not find any WWLLN match near this point  
189 within a reasonable time frame. Furthermore, according to simulations, the observed TEB  
190 duration in this configuration should be substantially longer than the observation (dis-  
191 cussed in next section).

192 Figure 3.a. shows an image of the thunderstorm system located around the north  
193 magnetic field line footprint, obtained by the geostationary satellite GOES-16 and has  
194 0.5 km spatial resolution (Advanced Baseline Imager band 2, visible red, centered at 0.64  
195  $\mu\text{m}$ ). The image was taken around 13:15:30 (UTC), i.e. about 45 seconds after the ASIM  
196 trigger. The positions of the three closeby WWLLN events are presented, and all are within  
197 6 ms of the ASIM trigger time. They also appear close to an overshooting top of the thun-  
198 derstorm system. Overshooting tops correspond to a region with high convective activ-  
199 ity, with a high lightning activity in the vicinity, therefore it is not surprising if this re-  
200 gion of the cloud generated a TGF.

201 Since this event shows a relatively low flux (i.e. particle count rate), instrumen-  
202 tal effects due to pulse pile-up and dead time are weak. It was possible to correct for them  
203 and get reliable energy calibration and count rates. MXGS HED and LED data from the  
204 ASIM Science Data Centre (in particular lightcurves and spectra) cannot be used for sci-  
205 entific analysis without performing mandatory post-processing step (including instru-  
206 mental effects corrections, calibration, and forward modeling using the Geant4 mass model),  
207 in collaboration with the ASIM-MXGS team. The energy spectrum of the event is pre-  
208 sented in Figure 5. The spectrum is actually softer than what is recorded during usual  
209 TGF events. The inset in Figure 5 shows a zoom below 780 keV using a finer binning,  
210 which reveals a line around 511 keV. This line is broader than the ones detected by the

211 Fermi space telescope (Briggs et al., 2011) due to different instrumental characteristics.  
212 A more detailed spectral analysis is presented in section 5.

#### 213 4 Monte-Carlo simulations of the event

214 Numerical Monte-Carlo simulations were performed to reproduce the recorded lightcurves  
215 and energy spectrum of the event. Two models were used to propagate the TGF and sec-  
216 ondary particles from the source of the TGF to ASIM: the MC-PEPTITA model (Sarria  
217 et al., 2015) and a new model based on the Geant4 toolkit (Agostinelli et al., 2003; Al-  
218 lison et al., 2006, 2016). The Geant4-based code is made publicly available (see acknowl-  
219 edgments) and presented into more details in appendix A. Both models are able to prop-  
220 agate photons, electrons and positrons in Earth's environment, including the atmosphere  
221 and the Earth's magnetic field. They include the relevant processes for photons (Comp-  
222 ton scattering, photo-electric absorption, pair production, Rayleigh scattering) and elec-  
223 tron/positron transport (elastic/inelastic scattering, bremsstrahlung, annihilation). For  
224 simplicity, we only show results from the Geant4-based model, as both models showed  
225 very consistent results in all the simulations we performed.

226 The simulations start from a time instantaneous photon source, with a bremsstrahlung  
227 energy spectrum  $\propto 1/\epsilon \times \exp(-\epsilon/7.3 \text{ MeV})$  (Dwyer et al., 2012). The TGF is located  
228 at 15 km altitude (later in this section an altitude range between 10 and 16 km is tested),  
229 pointing towards zenith, with an opening angle that can be isotropic or Gaussian. The  
230 isotropic angular distribution is parameterized by the opening half-angle  $\theta$ , and the Gaus-  
231 sian by the standard deviation  $\sigma_\theta$ . The time reference is set to the source TGF produc-  
232 tion time, assumed to be located at the coordinates of the northern or southern mag-  
233 netic footpoints. Figure 1 illustrates the geometry of the simulation, and explains why  
234 TEBs are temporally more dispersed than TGFs, and shows the pitch angle distribution  
235 as a function of arrival time that was obtained for this event. For a source TGF located  
236 at the north footpoint ( $\lambda = 11.076^\circ$ ,  $\phi = -95.399^\circ$ ), it takes about 2.28 ms for a di-  
237 rect photon (straight line) to travel from their source to the ISS (located about 650 km  
238 away), and the fastest electron/positron arrives about 48  $\mu\text{s}$  later. The pointing angle  
239 between the ISS and the TGF source is about  $58.4^\circ$  with respect to nadir. The positron  
240 to electron ration of the TEB when it hits the ISS is about 13%. Simulated data indi-  
241 cate that 95% of the electron/positron beam is contained in an ellipse of semi-major axis

242 of  $\approx 88$  km and semi-minor axis of  $\approx 54$  km. For simplicity, we will consider in the fol-  
243 lowing that the TEB is contained inside a circle, of about 70 km radius.

## 244 5 Discussion

245 Figure 2.a. presents a comparison between the observed lightcurve, and the sim-  
246 ulations. For all the simulations, except the green histogram, we assumed that the TGF  
247 was produced close to the northern footpoint of the magnetic field line that intercepts  
248 the ISS location. The simulated TEB lightcurve (electrons/positrons) is compatible with  
249 the measurement. Here, the simulated photon lightcurve is arbitrarily scaled to have its  
250 maximum (that is located about 2.2 ms) at the same level as the maximum of the elec-  
251 tron/positron lightcurve. The real relative amplitude between the two histograms is a  
252 function of the beaming angle of the source TGF and is discussed later.

253 TEB events may present a mirror pulse in some configurations. This is because charged  
254 particles moving in a converging magnetic field (i.e. a stronger field) are subject to the  
255 magnetic mirror "force" and are reflected. For this event, the IGRF-12 model gives a ge-  
256 omagnetic field magnitude at the northern footpoint (at 45 km altitude) of 34590 nT,  
257 and a weaker field of 29949 nT (-13.4%) at the southern (i.e. opposite) footpoint, hence  
258 no mirror pulse is expected. The lightcurve presented in Figure 2 does not present any  
259 mirror pulse indeed. There is a small count rate increase around 13 ms, that is consis-  
260 tent with background fluctuations. According to our calculation (time of travel along the  
261 field line), an hypothetical mirror pulse would be located much later, somewhere between  
262 60 and 75 ms.

263 In principle, TEBs could be also detected when they are produced in the opposite  
264 hemisphere (i.e. the southern hemisphere in this case). In Figure 2.a., the green histogram  
265 presents the lightcurve that would be observed if the TGF had been produced in the south-  
266 ern footpoint of the magnetic field line, and shows a signal about 4 times longer than the  
267 observation ( $\sim 20$  ms compared to  $\sim 5$  ms). Figure 2.b. shows the same lightcurves  
268 as 2.a., but zoomed-in between 2.1 and 3.1 ms. According to the simulation, the signal  
269 due to the photons from the TGF (produced  $\approx 650$  km away from the ISS) should be  
270 above the background level, and have a  $t_{90}$  duration of about 150 microseconds, for pho-  
271 tons above 400 keV (reminder: we assume, for now, an instantaneous TGF at source).  
272 The pulse due to TGF photons is about 20 times shorter than the one due to the TEB,

273 that lasts about 5 milliseconds. It indicates that some of the direct photons from the TGF  
 274 may also have been detected. This fraction will depend on the location of the ISS with  
 275 respect to the center of the electron/positron beam and, more importantly, on the an-  
 276 gular distribution of the TGF.

277 Figure 4.a. and b. presents the same comparison as before, but assuming several  
 278 angular distributions for the source TGF. Compared to figure 2, the relative effective ar-  
 279 eas of MXGS to detect photons ( $\sim 650 \text{ cm}^2$ ) and electrons/positrons ( $\sim 150 \text{ cm}^2$ ) is  
 280 also taken into account. MXGS-HED is actually about 4.33 times more efficient to de-  
 281 tect signal generated from incoming TGF photons than from TEB electrons and positrons.  
 282 A change in the TGF angular distribution parameter mostly affects the counts inside the  
 283 bin of the histogram located between 2.09 and 2.29 ms, containing mainly photons. . A  
 284 wider angular distribution of the source TGF implies that the relative amount of pho-  
 285 tons compared to electrons/positrons is increasing. A value of the angular parameter ( $\theta$   
 286 or  $\sigma_\theta$ ) is considered compatible with the measurement if the photon (red) bin count be-  
 287 tween 2.09 and 2.29 ms lies inside the  $1\text{-}\sigma$  error interval of the ASIM measurement in  
 288 the same bin. For the isotropic (within a cone) angular distribution, the observed lightcurve  
 289 is compatible with the simulations if a half-angle of  $\theta$  between  $30.6^\circ$  and  $41.9^\circ$  is used.  
 290 For the Gaussian angular distribution, it is for a  $\sigma_\theta$  between  $20.6^\circ$  and  $29.8^\circ$ . This range  
 291 is in agreement with previous studies (Dwyer & Smith, 2005; Østgaard et al., 2008; Hazel-  
 292 ton et al., 2009; Carlson et al., 2011; Mailyan et al., 2016). This scenario implies that  
 293 about 3.5 to 10 % of the recorded counts by ASIM-MXGS are actually direct TGF pho-  
 294 tons, that arrive mostly at the beginning of the recorded lightcurve.

295 The previous results have been obtained assuming an instantaneously produced source  
 296 TGF. But we also investigated the effects of using longer source TGF durations. We found  
 297 that the constraint on the angular distribution is similar for any source duration  $t_{90}^s <$   
 298  $197 \mu\text{s}$ , that corresponds to a recorded  $t_{90}^d < 260 \mu\text{s}$  after propagation to the satellite.  
 299 It is probably the case, because according to the TGF duration distribution obtained from  
 300 ASIM,  $\approx 90\%$  of the  $t_{90}$  durations are below  $260 \mu\text{s}$  (Østgaard et al., 2019). For longer  
 301 source durations, it is impossible to constraint the angular distribution using the method  
 302 presented above. This discussion is presented in more detail in appendix B.

303 Figure 5 presents a comparison between the recorded energy spectrum (background-  
 304 subtracted) and simulations, using a strategy of forward modeling. Two scenarios are

305 considered, one assuming that the incoming particles are photons from the TGF, and  
 306 the other assuming that the incoming particles are the secondary electron/positrons from  
 307 the TEB. The TGF and TEB spectra are first calculated using the Geant4-based model  
 308 of TGF propagation in the atmosphere with the assumptions presented previously (see  
 309 Section 4, and Appendix A). The particles are gathered at 400 km altitude, around the  
 310 position of the ISS ( $\pm 70$  km). We verified that the TEB spectrum does not change sig-  
 311 nificantly as a function of radial distance from its center (the corresponding data and  
 312 figures are presented in the associated data repository, see acknowledgments). The re-  
 313 sults of this first simulation are then used as input for the ASIM Geant4 mass model (pre-  
 314 sented by Østgaard et al. (2019)), and a set of simulated MXGS-HED spectra are pro-  
 315 duced. The quality of the simulated data compared to the observation can be quanti-  
 316 fied using the reduced chi squared ( $\chi_{red}^2$ ). The  $\chi_{red}^2$  values obtained for the simulated  
 317 response to a TGF and to a TEB are 7.2 and 1.13, respectively. Due to the chosen en-  
 318 ergy binning, there are 7 degrees of freedom, and using an usual 95% probability thresh-  
 319 old, it gives a critical value  $\chi_{red,c}^2$  equal to 2.01. It means that the TEB model, with  $\chi_{red}^2 <$   
 320  $\chi_{red,c}^2$ , is compatible with the measurement, whereas the TGF model, with  $\chi_{red}^2 >$   
 321  $\chi_{red,c}^2$ , is not. In addition to the results concerning the lightcurve (previous paragraph), and the  
 322 geographical and time lightning matches (section 3), we think that it is enough evidence  
 323 to consider that this event is mostly a TEB, with a small fraction (3.5% to 10%) of pho-  
 324 tons coming directly from the TGF.

325 Finally, we can estimate the required photons number  $N_\gamma$  of the source TGF in or-  
 326 der to obtain the  $\approx 160$  counts that were observed by HED. The exact value of  $N_\gamma$  de-  
 327 pends on assumptions of the source TGF, mainly the altitude of production and the an-  
 328 gular distributions. We performed a series of simulation using the Geant4-based model,  
 329 with a TGF altitude of production tested between 10 and 16 km, assuming an isotropic  
 330 distribution of photons within a cone (with parameter the half-angle of the cone,  $\theta$ , tested  
 331 from  $10^\circ$  to  $50^\circ$ ), or a Gaussian distribution (with parameter the standard deviation  $\sigma_\theta$ ,  
 332 tested from  $10^\circ$  to  $40^\circ$ ). The results are presented in figure 6.

333 The derived constraint on the TGF photon number is based on the number of elec-  
 334 trons/positrons detected by ASIM-MXGS, and not the number of photons as it is usu-  
 335 ally done. Most of the electrons/positrons that are detected by ASIM-MXGS are pro-  
 336 duced between 40 and 100 km altitude, along the Earth's magnetic field line that is in-  
 337 tercepting the ISS location. Most of the electrons/positrons ( $> 95\%$  of the total number)

338 are within 70 km radial distance around the field line. By increasing the angular distri-  
 339 bution of the source TGF, a large fraction the added electron/positrons have no chance  
 340 to reach ASIM since they are not produced close enough to the field line. In other words,  
 341 increasing the value of the beaming angle mostly adds new photons that will not con-  
 342 tribute to the TEB. Therefore the dependence of  $N_\gamma$  on  $\theta$  (when a source altitude is fixed)  
 343 can be approximated as being proportional to the solid angle of a cone, i.e.  $N_\gamma(\theta) \propto$   
 344  $\sin^2(\theta/2)$  ( $\theta$  is a half angle). This was checked to fit quite accurately the profile of  $N_\gamma(\theta)$ ,  
 345 at a fixed source altitude. At a fixed opening angle, the variation of  $N_\gamma$  with altitude is  
 346 directly linked to the absorption of the air. The absorption that has to be considered,  
 347 i.e. that will affect the number of produced electrons/positrons, is happening between  
 348 the source altitude and about  $h_l = 40$  km altitude. The integrated densities  $H$  that the  
 349 TGF photons have to cross before reaching  $h_l$  are about 290.41, 215.60, 156.18 and 111.05  
 350 g/cm<sup>2</sup> for source TGFs at altitudes of 16, 14, 12 and 10 km respectively. The photons  
 351 get absorbed about 80.5 times more for a source at 10 km altitude, compared to a source  
 352 at 16 km. This ratio is 14.0 for a source at 12 km altitude, and 3.46 for a source at 14  
 353 km altitude. The profile of relative absorption can be obtained with  $A(h) \propto \exp(-H(h) \mu/\rho)$   
 354 and using an effective mass-energy absorption coefficient  $\mu/\rho \approx 0.0247$  cm<sup>2</sup>/g. This value  
 355 corresponds to the coefficient for air for photons at about 1.7 MeV, that is approximately  
 356 the average of the assumed source TGF energy profile, if integrated between 60 keV and  
 357 40 MeV.

358 If the constraints on the angular distributions are considered (discussed before),  
 359 a value of  $N_\gamma$  of  $10^{17.2}$  (high altitude) up to  $10^{18.9}$  photons (low altitude) is required to  
 360 reproduce the particle count measured by ASIM-MXGS-HED (see Figure 6). This range  
 361 is in agreement with values given by previous studies (Dwyer & Smith, 2005; Dwyer et  
 362 al., 2012; Cummer et al., 2014; Gjesteland et al., 2015; Mailyan et al., 2016).

## 363 6 Conclusions and future work

364 We report the first TEB detected by the MXGS-HED instrument on-board the Atmosphere-  
 365 Space Interactions Monitor (ASIM). It appeared as an unusually long event ( $> 2$  ms)  
 366 with a spectrum softer than what is usually seen from TGF events. Tracing of the ge-  
 367 omagnetic field line from the ISS permitted to estimate a likely geographical position of  
 368 the TGF that produced the TEB, where three WWLLN matches within compatible time  
 369 ( $< 6$  ms) and distance ( $< 15$  km) intervals were found. From geostationary imaging, ob-

370 tained just about 45 seconds after the event, it appears that the TGF was produced in  
371 the vicinity of an overshooting top of a thunderstorm.

372 Using Monte-Carlo simulations to reproduce the observed lightcurve and energy  
373 spectrum, we show that the event is indeed mostly explained by a TEB, even if 3.5% to  
374 10% of the detected flux may be direct TGF photons. A source TGF with a broad an-  
375 gular distribution can explain the observation ( $\theta \approx 30.6^\circ - 41.9^\circ$  for a isotropic within  
376 cone distribution, or  $\sigma_\theta \approx 20.6^\circ - 29.8^\circ$  for a Gaussian distribution). This constraint  
377 is valid only if the source TGF has a duration  $t_{90}^s < 197 \mu s$  (that corresponds to a du-  
378 ration at satellite altitude of  $t_{90}^s = 260 \mu s$ ). This is a likely possibility according to the  
379 distribution of TGF durations recorded by ASIM, where 90% of the TGFs have a  $t_{90} <$   
380  $260 \mu s$  (see Østgaard et al. (2019), Figure 2). In addition, the intensity of the source TGF  
381 could be estimated for various assumptions of the source (altitude of production, angu-  
382 lar distribution), and is between  $10^{17.2}$  and  $10^{18.9}$  photons. This range is in agreement  
383 with previous studies.

384 Here, we have discussed a TEB event detected during the daytime by the HED in-  
385 strument alone. Future observations during nighttime have the added promise of simul-  
386 taneous detection by the LED and MMIA instruments. It will allow measurements of  
387 the low-energy part of the spectrum ( $\sim 70$  keV to  $\sim 400$  keV), and hypothetical UV and  
388 optical emissions associated with such events.

389 Planned for a launch in 2020, the TARANIS micro-satellite (Lefeuvre et al., 2009),  
390 should also detect TEB events. It is primarily designed to detect both TGFs and TEBs,  
391 with help of the XGRE and IDEE instruments (Sarria et al., 2017), and will have, in ad-  
392 dition, the capability of detecting hypothetical radio emissions from TEBs.

## 393 7 Acknowledgments

394 This work was supported by the European Research Council under the European  
395 Union's Seventh Framework Program (FP7/2007-2013)/ERC grant agreement n. 320839  
396 and the Research Council of Norway under contract 223252/F50 (CoE). ASIM is a mis-  
397 sion of ESA's SciSpace Programme for scientific utilization of the ISS and non-ISS space  
398 exploration platforms and space environment analogues. This study has received fund-  
399 ing from the European Union's Horizon 2020 research and innovation programme un-  
400 der the Marie Skłodowska-Curie grant agreement SAINT 722337. ASIM was funded through

401 the ESA ELIPS program, through contracts with TERMA and Danish Technical Uni-  
402 versity (DTU) in Denmark, University of Bergen (UB) in Norway and University of Va-  
403 lencia (UV) in Spain. Additional funding was supported by the ESA PRODEX contracts  
404 PEA 4000105639 and 4000111397 to DTU and ESA PRODEX contract 4000102100 and  
405 by Norwegian Research Council to UB. The ASIM Science Data Centre (ASDC) at DTU  
406 is supported by PRODEX contract PEA 4000115884 and by PRODEX contract PEA4000123438  
407 at UB. The ASIM Science Data Centre and data analysis activities at the UV are sup-  
408 ported by the MINECO Research Grants ESP2015- 69909-C5-1-R and ESP2017-86263-  
409 C4-1-R.

410 The GOES-R Advanced Baseline Imager data are available via the National Oceanic  
411 and Atmospheric Administration (NOAA) Comprehensive Large Array-data Steward-  
412 ship System (CLASS).

413 The simulations were performed on resources provided by UNINETT Sigma2 - the  
414 National Infrastructure for High Performance Computing and Data Storage in Norway,  
415 under project no. NN9526K.

416 The Geant4-based model for Terrestrial Gamma-ray Flash (TGF) and associated  
417 electrons and positrons propagation in Earth atmosphere and environment (magnetic  
418 field) is available in the following GitHub repository: [https://github.com/DavidSarria89/  
419 TGF-Propagation-Geant4](https://github.com/DavidSarria89/TGF-Propagation-Geant4), or the DOI: <https://doi.org/10.5281/zenodo.2597039>.

420 The data described in this paper is available in the following repository [https://  
421 github.com/DavidSarria89/asim-teb-paper-1-data-repo](https://github.com/DavidSarria89/asim-teb-paper-1-data-repo), or the DOI: [https://doi  
422 .org/10.5281/zenodo.3395472](https://doi.org/10.5281/zenodo.3395472).

423 We thank the World-Wide Lightning Location Network (WWLLN) team and the  
424 institutions contributing to WWLLN. WWLLN data cannot be freely distributed. Spe-  
425 cific WWLLN data entries within a second around the ASIM 180916 TEB/TGF event  
426 are provided in the associated data repository (see above).

	Time (UTC)	$\lambda(^{\circ})$	$\phi(^{\circ})$	$h$ (km)		
Magnetic foot point	N.A.	11.076	-95.399	45		
International Space Station	13:14:44.733601	6.281	-95.709	402.5	$\Delta t$ (ms) (vr trg. time)	$\Delta r$ (km) (vr mag. foot pt.)
WWLLN event #1	13:14:44.601058	6.370	-89.376	N.A.	132.543	895.77
WWLLN event #2	13:14:44.700633	6.414	-89.301	N.A.	32.968	899.78
WWLLN event #3	13:14:44.738894	11.028	-95.291	N.A.	-5.293	13.79
WWLLN event #4	13:14:44.738925	11.081	-95.288	N.A.	-5.324	12.69

**Table 1.** Summary table of the time and coordinates of the interesting elements for the ASIM

event that happened on 2018/09/16.  $\lambda$ ,  $\phi$  and  $h$  are latitude, longitude and altitude. All the given coordinates geodetic/geographic, using the WGS84 reference ellipsoid. WWLLN events number 3 and 4 are in a very narrow time (with respect to the event trigger time) and distance windows (with respect to the northern magnetic field line footpoint) and can be considered as good matches for the lightning discharge that produced the source TGF. Due to their very narrow time differences ( $< 0.1$  ms), these two matches probably belong to the same discharge.

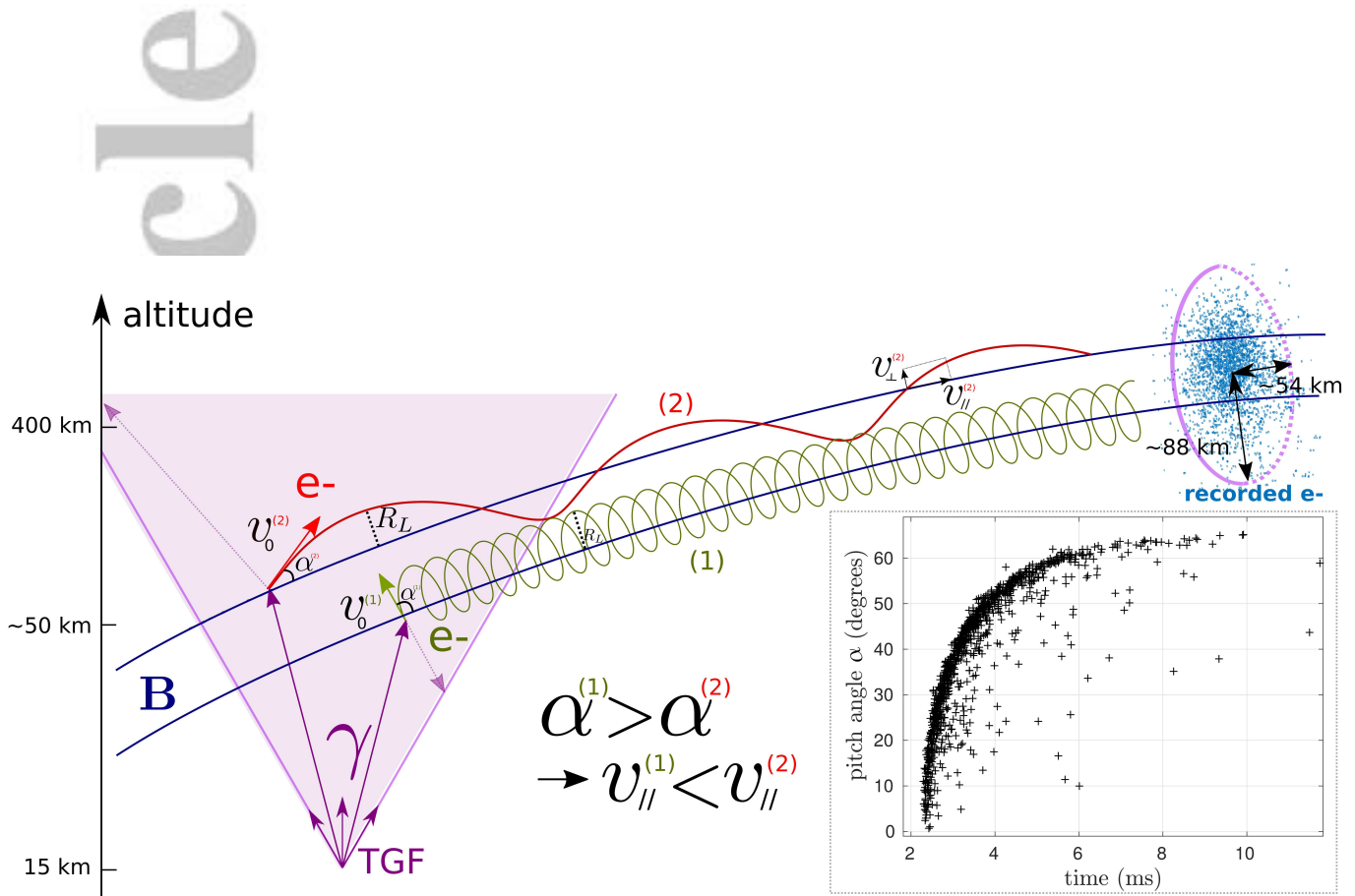


**Figure 1.** This sketch illustrates why the time distribution for a TEB event is mainly due to the pitch angle  $\alpha$  with respect to Earth’s magnetic field. Most of the electrons/positrons are relativistic and hence have a speed close to the speed of light. However, they have to follow helical trajectories around the field lines, and the electrons/positrons with larger  $\alpha$  will undergo more rotations around the field lines, and with a larger Larmor radius ( $R_L$ ) at the same electron energy, before reaching the satellite. They have actually a smaller velocity along the field line ( $v_{||}$ ). More energetic electrons will have a larger  $R_L$  (as it is proportional to the Lorentz’s  $\gamma$  factor). The insert shows the pitch angle as function of arrival time (according to the simulations described in section 4). At the satellite level, most of the electrons will arrive inside an ellipse of 54 km semi-minor axis and 88 km semi-major axis.

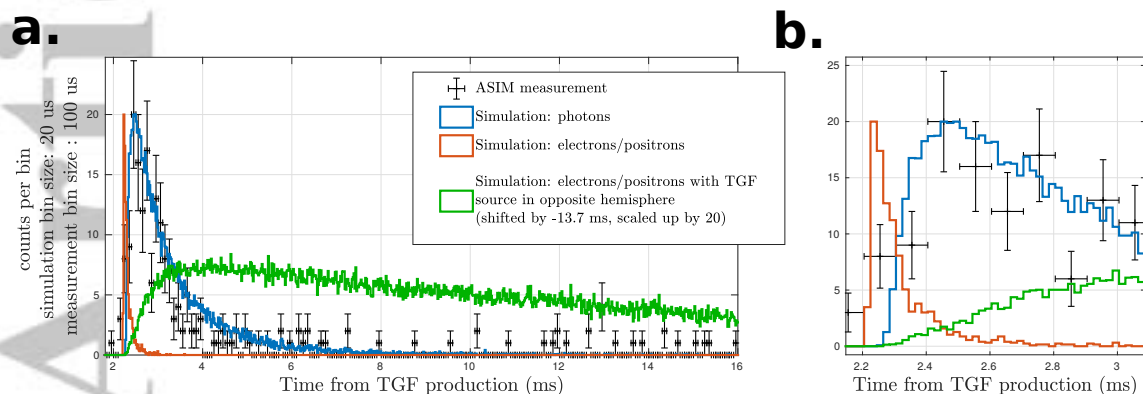


**Figure 2.** **a.** Comparison between simulated and measured lightcurves for the TEB event.

Error bars indicate a  $1\text{-}\sigma$  interval, and are calculated as the square root of the number of counts in each bin. Time 0 is when the source TGF is produced. The signal of the photons (TGF) and electrons/positrons (TEB) are shown. The simulated photon lightcurve (red) is scaled to have its maximum (that is located around 2.2 ms) at the same level as the maximum of the electron/positron lightcurve (blue).

The observed lightcurve matches the electron/positron component (TEB) of September 16th, 2018. The green histogram presents the TEB lightcurve that would be observed if the associated TGF was produced in the southern footpoint of the magnetic field line, and shows a signal about 5 times longer than the observation. It was scaled in amplitude by a factor of 20 and shifted in time by  $-13.7$  ms, to be able to display it inside the same time scale. **b.** Zoomed in between 2.1 and 3.1 ms. The simulations indicate that photons from the TGF could also have been observed, and they should be mostly within the first 0.2 ms of the event. According to this simulation, most of the recorded counts below about 2.3 ms are due to photons.

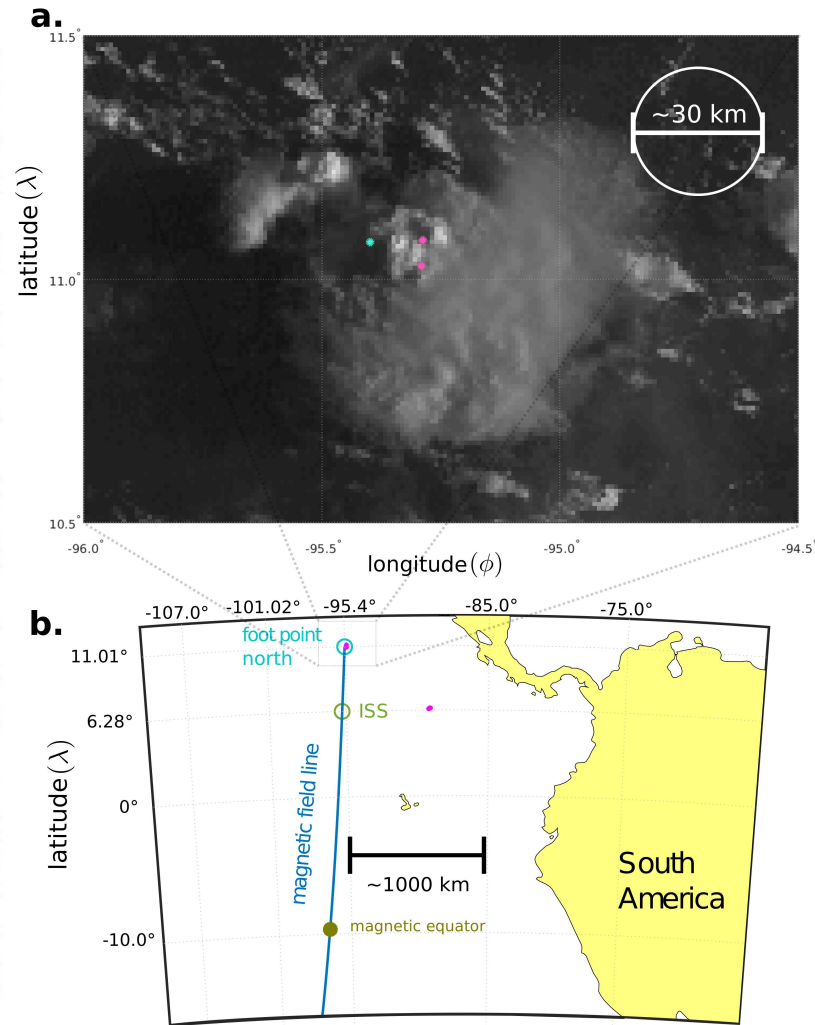


**Figure 3.** **a.** Image from geostationary satellite GOES-16 on September 16th, 2018, around 13:15:30 UTC (about 45 seconds after ASIM trigger time), zoomed around the north magnetic footpoint region. The image comes from the Advanced Baseline Imager instrument, optical band 2, centered at  $0.64 \mu\text{m}$ , with  $0.5 \text{ km}$  resolution. The cyan dot gives the position of the footpoint at  $45 \text{ km}$  altitude of the magnetic field line intercepting the ISS location. The two closest positions obtained from WWLLN are presented as magenta dots, that may correspond to a single discharge. They are within  $6 \text{ ms}$  of the ASIM trigger time (the MXGS absolute timing uncertainty is about  $20 \text{ ms}$ ) and within  $15 \text{ km}$  of the northern magnetic footpoint (the WWLLN generic positioning uncertainty is  $\pm 15 \text{ km}$ ). The two points are located close to an overshooting top of the thunderstorm system. **b.** The map shows the positions of interesting points of the event. The ISS (green dot) is located at a latitude  $\lambda = 6.28^\circ$  and a longitude  $\phi = -95.71^\circ$ . The red dot is located at the northern magnetic footpoint of the magnetic field line passing through the ISS (coordinates  $\lambda = 10.98^\circ$ ,  $\phi = -95.39^\circ$ ). The corresponding magnetic latitude is  $21.05^\circ$  (modified apex). The small magenta dots are the position of the lightning discharges obtained from WWLLN sferic detections, within a time frame of  $140 \text{ milliseconds}$  around the ASIM trigger time.

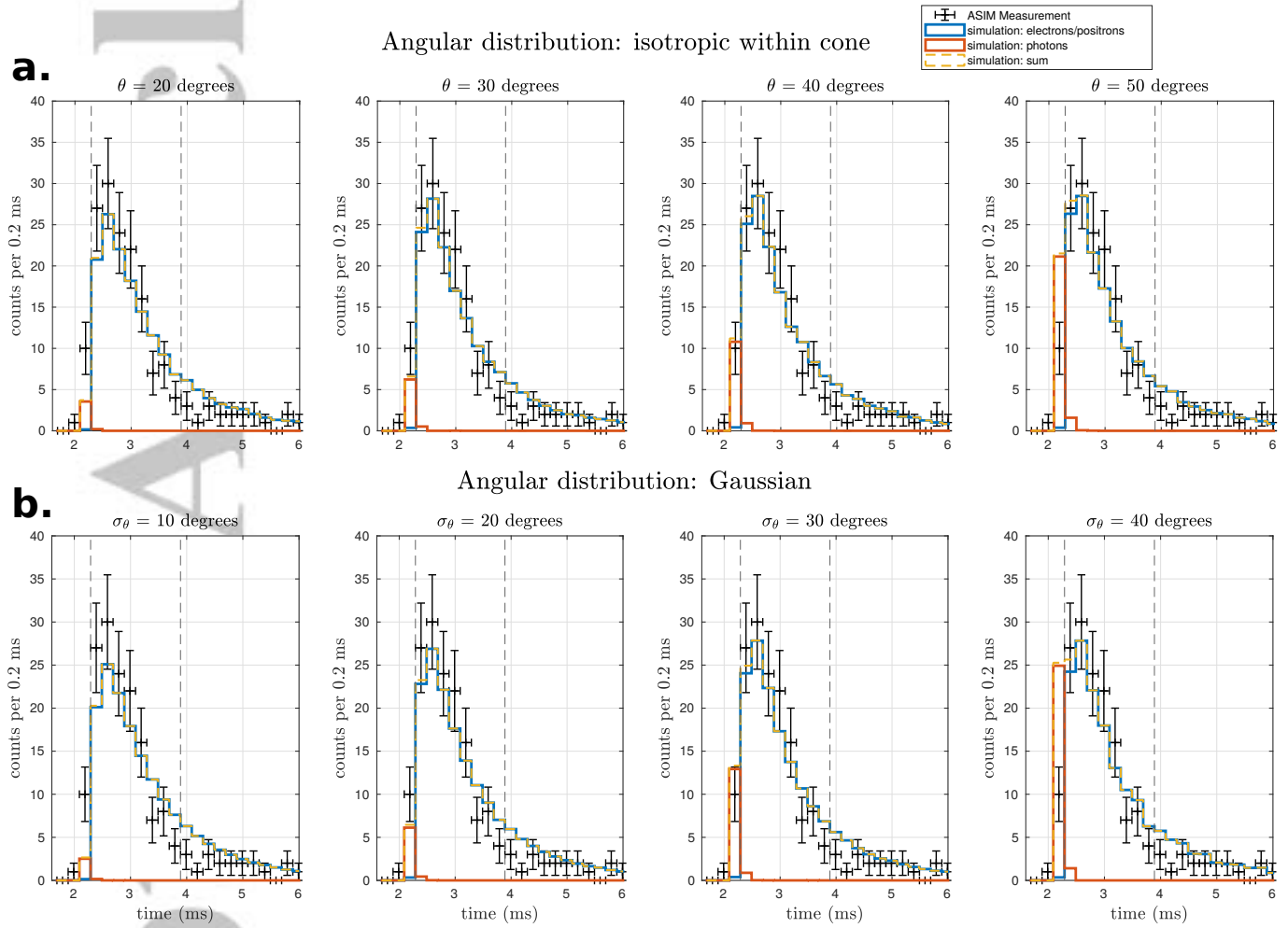


**Figure 4.** Comparison of the simulated and measured lightcurves, assuming various opening angles of the source TGF. Compared to figure 2, the relative fluxes between electrons/positrons and photons take now into account the efficiency of the detector for the different particles. Error bars indicate a  $1\text{-}\sigma$  interval, and are calculated as the square root of the number of counts in each bin. The simulation is scaled to the measurement to minimize the value of the  $\chi^2$ . The bins between 2.09 and 3.89 are used to compute it (shown with vertical dashed lines). A change in the source TGF opening angle mostly affects the photon (red) count rate between 2.09 and 2.29 ms. **a.** Isotropic angular distribution inside a cone, with half angle  $\theta$ . **b.** Gaussian angular distribution with standard deviation  $\sigma_\theta$ .

icle

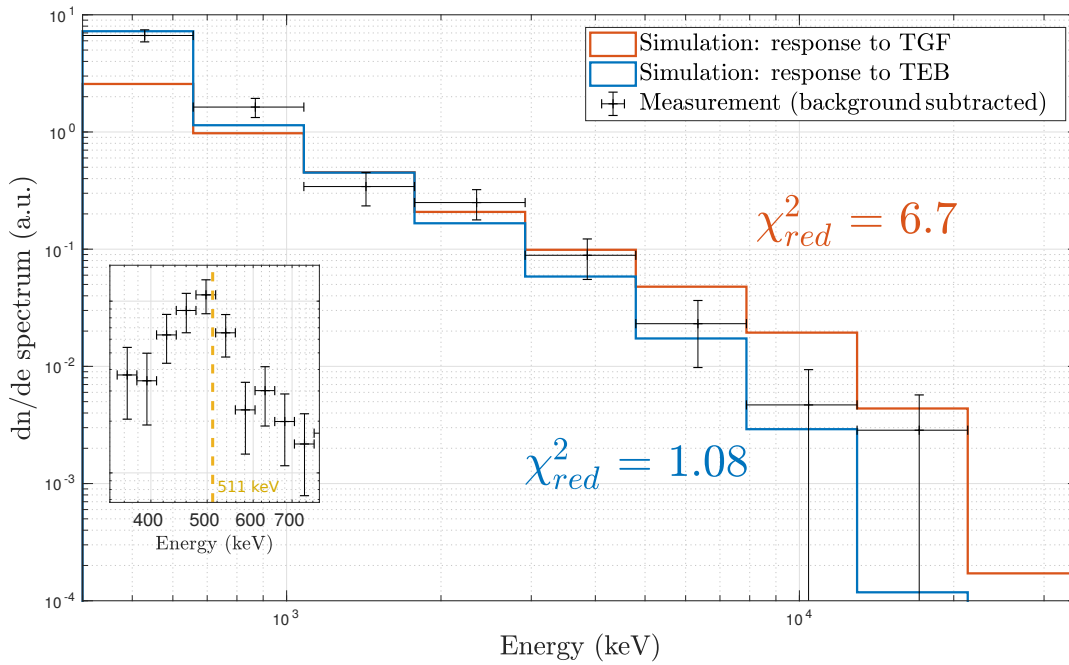


**Figure 5.** Energy spectrum comparison between the ASIM-MXGS measurement and simulations. The inset shows the recorded spectrum below 780 keV using a finer binning, which reveals a line around 511 keV. Two simulation scenarios were considered: incoming particles are from TGF or TEB. The two simulated spectra are scaled to minimize the values of  $\chi_{red}^2$ , and the minimum values obtained for each model are indicated.

Accepted

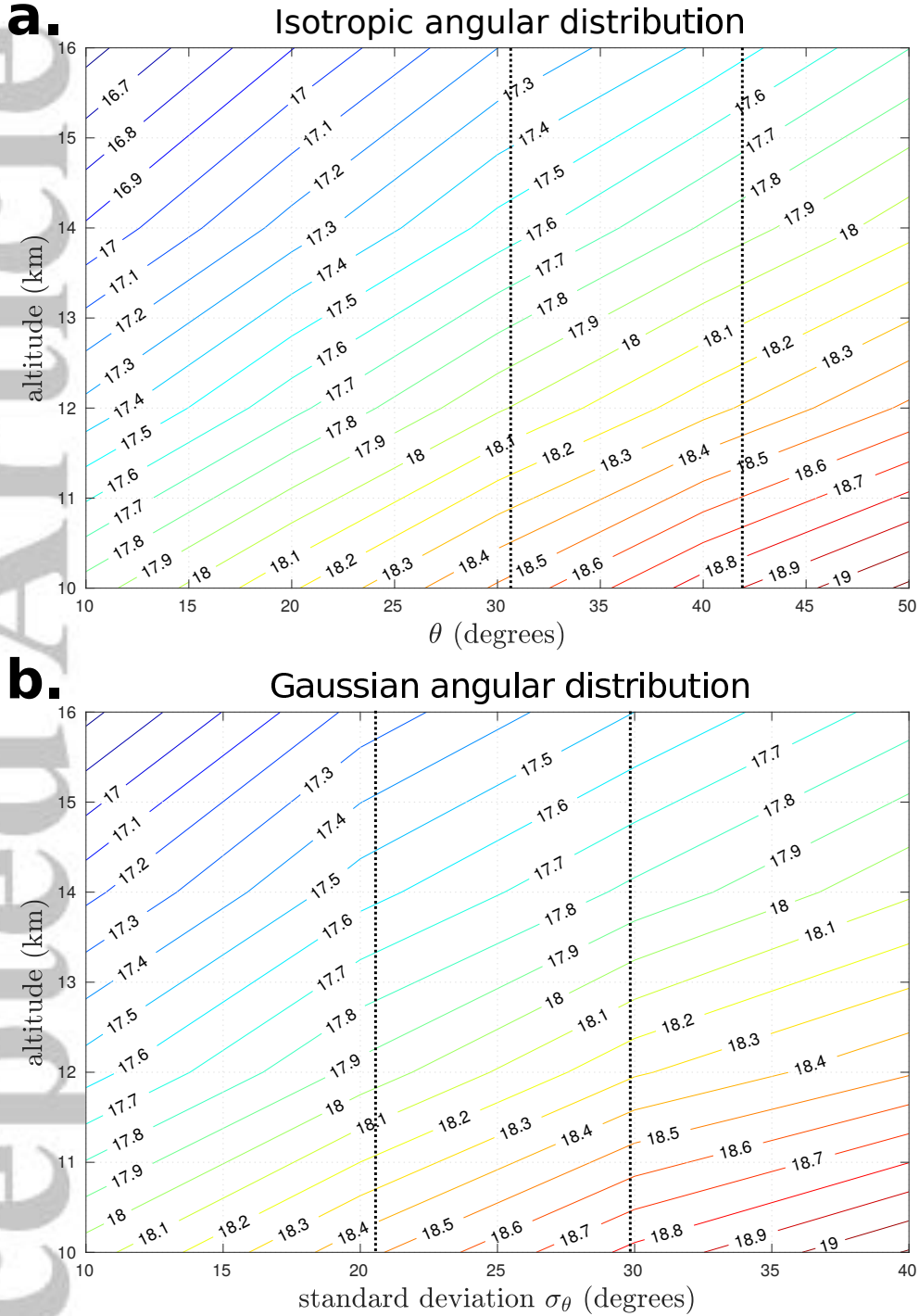


**Figure 6.** Level curves of the photon number intensity  $N_\gamma$  of the source TGF required for the simulation to produce the  $\approx 160$  counts recorded during the ASIM event 180916. It is expressed as function of altitude and opening angle, in decimal logarithm. The dotted lines demarcate the parameter space where the angular distribution has been constrained (see figure 4). **a.** Assuming that the source TGF has a isotropic angular distribution inside a cone, with half angle  $\theta$ . **b.** Assuming a Gaussian angular distribution with standard deviation  $\sigma_\theta$ .

## Appendix A Geant4-based Monte-Carlo model of TGF and TEB propagation in the atmosphere, ionosphere and magnetosphere.

In order to estimate the response of MXGS-HED instrument for this event, we first needed to generate TGF (photons) and TEB (electrons and positrons) spectra just before they reach the International Space Station. We used a code based on the Geant4 toolkit (Agostinelli et al., 2003; Allison et al., 2006, 2016) to propagate particles in the atmosphere, ionosphere and magnetosphere. The code is available in an online repository, see acknowledgments. The geometry uses 256 exponentially spaced atmospheric layers between 1 and 150 km altitude (the atmosphere is negligible above) of constant density, composed only of  $N_2$  and  $O_2$ , for simplicity and better performance. Densities within these layers are calculated with the NRLMSISE-00 model (Picone et al., 2002). The magnetic field of the Earth is modeled using the IGRF-12 model (Thébault et al., 2015). The propagation of photons, electrons and positrons is simulated, including all the relevant processes, which are included in the Geant4 toolkit. Different models can be used (semi-analytical, or database driven like Livermore or Penelope), more-or-less accurate in the low energy part. In the context of photon/electron/positron propagation in air above 50 keV, and without electric fields, they all show similar results as long as the effects of straggling are included (Rutjes et al., 2016), that is the default behavior of Geant4.

The source TGF is assumed to be a point source with adjustable altitude, typically set between 10 and 16 km. The energy spectrum has an exponential distribution proportional to  $1/\epsilon \exp(-\epsilon/\epsilon_{cut})$ , with a cutoff  $\epsilon_{cut} = 7.3$  MeV. The angular distribution is Gaussian with a standard deviation of 30 degrees, and has no tilt. The electrons, photons and positrons are collected at an altitude of 400 km, inside a circle of  $R = 80$  km radius around the position of the ISS. The spectra can be built using this data, but to properly build the photon lightcurve,  $R$  should be less than 1 km (to avoid artificial time broadening). Figure A1 shows the recorded energy spectra at 400 km altitude. They were then used as an input to calculate the response of the ASIM mass model to the TGF and the TEB. The electron energy spectrum can be fit by an exponential distributions ( $\propto \exp(-\epsilon/\epsilon_{cutoff})$ , where  $\epsilon$  is the energy). It results in cut-off energy of  $\epsilon_{cutoff} = 2.88 \pm 0.176$  MeV, that is compatible with the range of 2.3 to 4.6 MeV found by Briggs et al. (2011).

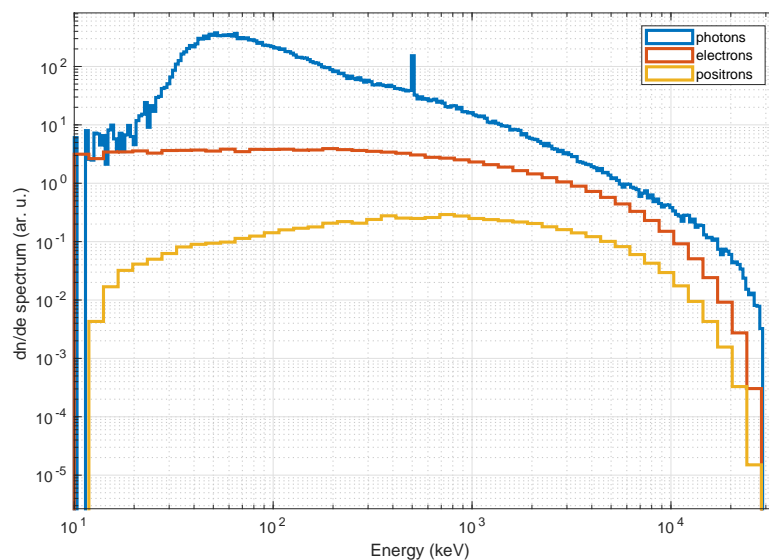


**Figure A1.** Results of the Geant4-based model simulation. Photon, electron and positron energy spectrum, recorded at 400 km altitude, within 70 km radial distance around the ISS position (i.e. in a plane perpendicular to the local vertical). The photon spectrum uses a finer binning to better represent the 511 keV line when this spectrum is used as input for the ASIM mass model. The source TGF is located at 15 km altitude and has a Gaussian angular distribution centered towards zenith with standard deviation of  $\sigma_{\theta} = 30^{\circ}$ . The amplitude of the spectra shown here is not representative of the fluence ratios (particles/cm<sup>2</sup>) of the different particle types.

459 The amplitude of the spectra shown in the figure are not representative of the flu-  
 460 ences (particles/cm<sup>2</sup>) of the different particle types. The fluence ratio of positrons over  
 461 electrons arriving to the ISS is about 13% in this case. For other settings of the source  
 462 altitude or the angular distribution, it can fluctuate between 11% and 16%. The fluence  
 463 ratio of electrons+positrons over photons arriving at the ISS is dependent on where the  
 464 satellite is located with respect to the center of the TEB, on the offset between the TEB  
 465 and the TGF (which depends on the geographical location) and on the angular distri-  
 466 bution of the TGF. Figure A2 presents the evolution of this ratio as function of the dis-  
 467 tance to the center of the electron beam, for an initial TGF with a Gaussian angular dis-  
 468 tribution with several values of  $\sigma_{\theta}$ .

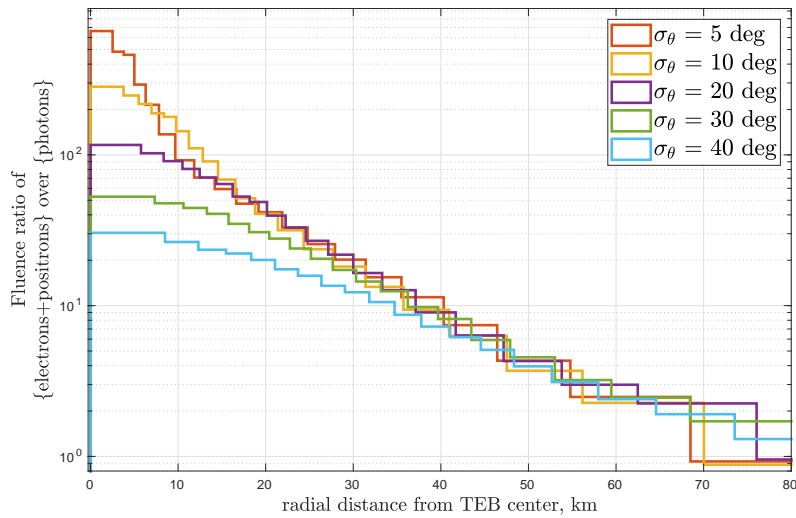


**Figure A2.** Fluence ratio between electrons+positrons (TEB) and photons (TGF) arriving at the ISS, according to the simulation. In this case, the ISS is located at about 650 km of the source TGF. The fluence ratio is presented as function of the distance between the ISS and the center of the electron beam, for several angular distributions (assuming a Gaussian distribution with parameter  $\sigma_\theta$ ). The source TGF is located at 15 km altitude. The response of the MXGS detector (i.e. the relative detection efficiency between electrons and photons) is not taken into account here. Note that the real spatial distribution of the leptons is contained inside an ellipse and here the particles are recorded inside rings (circular symmetry) for simplicity.

## Appendix B Effect of longer TGF source durations on the angular distribution constraint.

In this appendix, we provide a comprehensive discussion on the effects of assuming a longer TGF source duration ( $t_{90}^s$ ) on the constraint on the angular distribution. If the TGF source duration is too long, it will blur (or smear) both the detected TGF and the TEB lightcurves, and could lead to different conclusions regarding the presented constraint on the beaming angle. We want to determine what is the maximum allowed value of  $t_{90}^d$  for the conclusions to be still valid.

First, it is important to distinguish between  $t_{90}^d$ , the detected TGF duration (when the TGF is detected by a satellite) and  $t_{90}^s$ , the source (or intrinsic, i.e. when the TGF is produced), because the propagation in the atmosphere implies a spread (or smearing) of the duration (and this spread is larger if the radial distance between the TGF source point and the sub-satellite point is larger; it also depends on the considered photon energy range). We always have  $t_{90}^d > t_{90}^s$ . According to the simulation, assuming an instantaneous source ( $t_{90}^s = 0$ ), the detected TGF  $t_{90}^d$  duration is about  $150 \mu\text{s}$  in this case (the radial distance between the TGF source point and the sub-satellite point is about 650 km). We can model the source TGF duration with a Gaussian (normal) distribution with parameter  $\sigma_t^{TGF}$ . Note that the  $t_{90}^s$  duration of the gaussian time profile is directly linked to  $\sigma_t^{TGF}$  by  $t_{90}^s = 3.290 \sigma_t^{TGF}$  (and  $t_{50}^s = 1.349 \sigma_t^{TGF}$ ). For simplicity, we only show here the results for the Gaussian angular distribution.

Figure B1 presents how the lightcurves are changing with different  $\sigma_t^{TGF}$ . When  $\sigma_t^{TGF}$  is increased, the simulated lightcurves get too much smeared (spread out) compared to the measurement. This effect can be quantified by looking at the reduced  $\chi^2$  value between the simulation and the measurement. The value of  $\chi_{red}^2$  as function of  $\sigma_t^{TGF}$  is presented in figure B2. Only the bins between 2.29 and 3.89 ms are kept for the  $\chi^2$  calculation (that are shown by the dashed vertical lines in Figure B1). An instantaneous TGF source ( $\sigma_t^{TGF} = 0$ ) gives the best fit to the lightcurve, and increasing it gives less accurate ones. However, if we perform a  $\chi^2$  test, only  $\sigma_t^{TGF}$  values above 0.242 ms are rejected, using a standard 95% probability threshold.

In section 5, we established a constrain on the beaming angle by assuming that the beginning of the recorded lightcurve (i.e. the bin between 2.09 and 2.29 ms) contains mostly photons. This assumption will not be true anymore after increasing  $\sigma_t^{TGF}$  above a cer-

cle

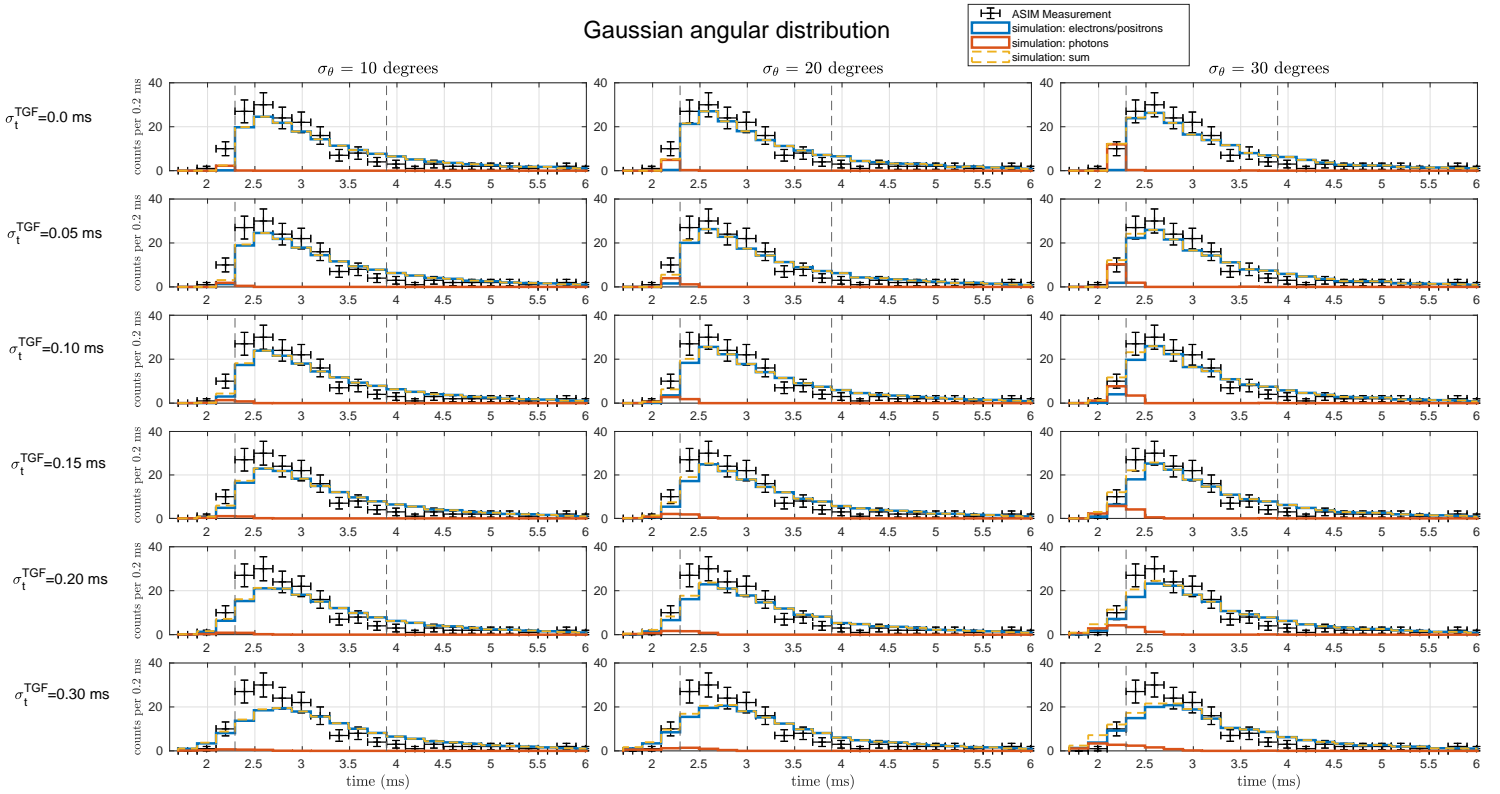


**Figure B1.** Comparison of the simulated (photons, electrons/positrons, and sum of both components) and measured lightcurves, assuming various opening angles and source duration of the source TGF. Error bars indicate a  $1\text{-}\sigma$  interval, and are calculated as the square root of the number of counts in each bin. The simulations are scaled to the measurement to minimize  $\chi^2$ . The dashed vertical lines indicate the time interval ( $2.29 \text{ ms} < t < 3.89 \text{ ms}$ ) where the  $\chi^2$  calculation is done (see Figure B2 for the results)

Accepted



518 **References**

- 519 Agostinelli, S., Allison, J., Amako, K., Apostolakis, J., Araujo, H., Arce, P., . . .  
 520 others (2003, July). GEANT4 - a simulation toolkit. *Nuclear Instru-*  
 521 *ments and Methods in Physics Research A*, 506, 250-303. doi: 10.1016/  
 522 S0168-9002(03)01368-8
- 523 Allison, J., Amako, K., Apostolakis, J., Araujo, H., Dubois, P. A., Asai, M., . . .  
 524 others (2006, February). Geant4 developments and applications. *IEEE Trans-*  
 525 *actions on Nuclear Science*, 53, 270-278. doi: 10.1109/TNS.2006.869826
- 526 Allison, J., Amako, K., Apostolakis, J., Arce, P., Asai, M., Aso, T., . . . Yoshida,  
 527 H. (2016, November). Recent developments in GEANT4. *Nuclear*  
 528 *Instruments and Methods in Physics Research A*, 835, 186-225. doi:  
 529 10.1016/j.nima.2016.06.125
- 530 Briggs, M. S., Connaughton, V., Wilson-Hodge, C., Preece, R. D., Fishman, G. J.,  
 531 Kippen, R. M., . . . Smith, D. M. (2011, January). Electron-positron beams  
 532 from terrestrial lightning observed with Fermi GBM. *Geophys. Res. Lett.*, 38,  
 533 L02808. doi: 10.1029/2010GL046259
- 534 Briggs, M. S., Fishman, G. J., Connaughton, V., Bhat, P. N., Paciasas, W. S.,  
 535 Preece, R. D., . . . Chekhtman, A. (2010, July). First results on terrestrial  
 536 gamma ray flashes from the Fermi Gamma-ray Burst Monitor. *Journal of Geo-*  
 537 *physical Research (Space Physics)*, 115, A07323. doi: 10.1029/2009JA015242
- 538 Carlson, B. E., Gjesteland, T., & Østgaard, N. (2011, November). Terres-  
 539 trial gamma-ray flash electron beam geometry, fluence, and detection fre-  
 540 quency. *Journal of Geophysical Research (Space Physics)*, 116, A11217. doi:  
 541 10.1029/2011JA016812
- 542 Chanrion, O., Neubert, T., Lundgaard Rasmussen, I., Stoltze, C., Tcherniak, D.,  
 543 Jessen, N. C., . . . Lorenzen, M. (2019, June). The Modular Multispectral  
 544 Imaging Array (MMIA) of the ASIM Payload on the International Space Sta-  
 545 tion. *Space Sci. Rev.*, 215, 28. doi: 10.1007/s11214-019-0593-y
- 546 Cohen, M. B., Inan, U. S., Said, R. K., Briggs, M. S., Fishman, G. J., Connaughton,  
 547 V., & Cummer, S. A. (2010, Sep). A lightning discharge producing a beam  
 548 of relativistic electrons into space. *Geophys. Res. Lett.*, 37(18), L18806. doi:  
 549 10.1029/2010GL044481
- 550 Cummer, S. A., Briggs, M. S., Dwyer, J. R., Xiong, S., Connaughton, V., Fishman,

- 551 G. J., ... Solanki, R. (2014, December). The source altitude, electric current,  
552 and intrinsic brightness of terrestrial gamma ray flashes. *Geophys. Res. Lett.*,  
553 *41*, 8586-8593. doi: 10.1002/2014GL062196
- 554 Dwyer, J. R., Grefenstette, B. W., & Smith, D. M. (2008, January). High-energy  
555 electron beams launched into space by thunderstorms. *Geophys. Res. Lett.*, *35*,  
556 L02815. doi: 10.1029/2007GL032430
- 557 Dwyer, J. R., & Smith, D. M. (2005, November). A comparison between Monte  
558 Carlo simulations of runaway breakdown and terrestrial gamma-ray flash ob-  
559 servations. *Geophys. Res. Lett.*, *32*, L22804. doi: 10.1029/2005GL023848
- 560 Dwyer, J. R., Smith, D. M., & Cummer, S. A. (2012, November). High-Energy At-  
561 mospheric Physics: Terrestrial Gamma-Ray Flashes and Related Phenomena.  
562 *Space Sci. Rev.*, *173*, 133-196. doi: 10.1007/s11214-012-9894-0
- 563 Emmert, J. T., Richmond, A. D., & Drob, D. P. (2010, August). A computationally  
564 compact representation of Magnetic-Apex and Quasi-Dipole coordinates with  
565 smooth base vectors. *Journal of Geophysical Research (Space Physics)*, *115*,  
566 A08322. doi: 10.1029/2010JA015326
- 567 Fishman, G. J., Bhat, P., Malozzi, R., Horack, J., Koshut, T., Kouveliotou, C., ...  
568 others (1994). Discovery of intense gamma-ray flashes of atmospheric origin.  
569 *Science-AAAS-Weekly Paper Edition-including Guide to Scientific Informa-*  
570 *tion*, *264*(5163), 1313-1316.
- 571 Gjesteland, T. (2012). *Properties of Terrestrial Gamma ray Flashes. Modelling and*  
572 *Analysis of BATSE and RHESSI data* (Doctoral dissertation, The University  
573 of Bergen). Retrieved from <http://bora.uib.no/handle/1956/6203>
- 574 Gjesteland, T., Østgaard, N., Laviola, S., Miglietta, M. M., Arnone, E., Marisaldi,  
575 M., ... Montanya, J. (2015, December). Observation of intrinsically bright  
576 terrestrial gamma ray flashes from the Mediterranean basin. *Journal of Geo-*  
577 *physical Research (Atmospheres)*, *120*, 12. doi: 10.1002/2015JD023704
- 578 Hazelton, B. J., Grefenstette, B. W., Smith, D. M., Dwyer, J. R., Shao, X.-M., Cum-  
579 mer, S. A., ... Holzworth, R. H. (2009, January). Spectral dependence of  
580 terrestrial gamma-ray flashes on source distance. *Geophys. Res. Lett.*, *36*,  
581 L01108. doi: 10.1029/2008GL035906
- 582 Hutchins, M. L., Holzworth, R. H., Brundell, J. B., & Rodger, C. J. (2012, Dec).  
583 Relative detection efficiency of the World Wide Lightning Location Network.

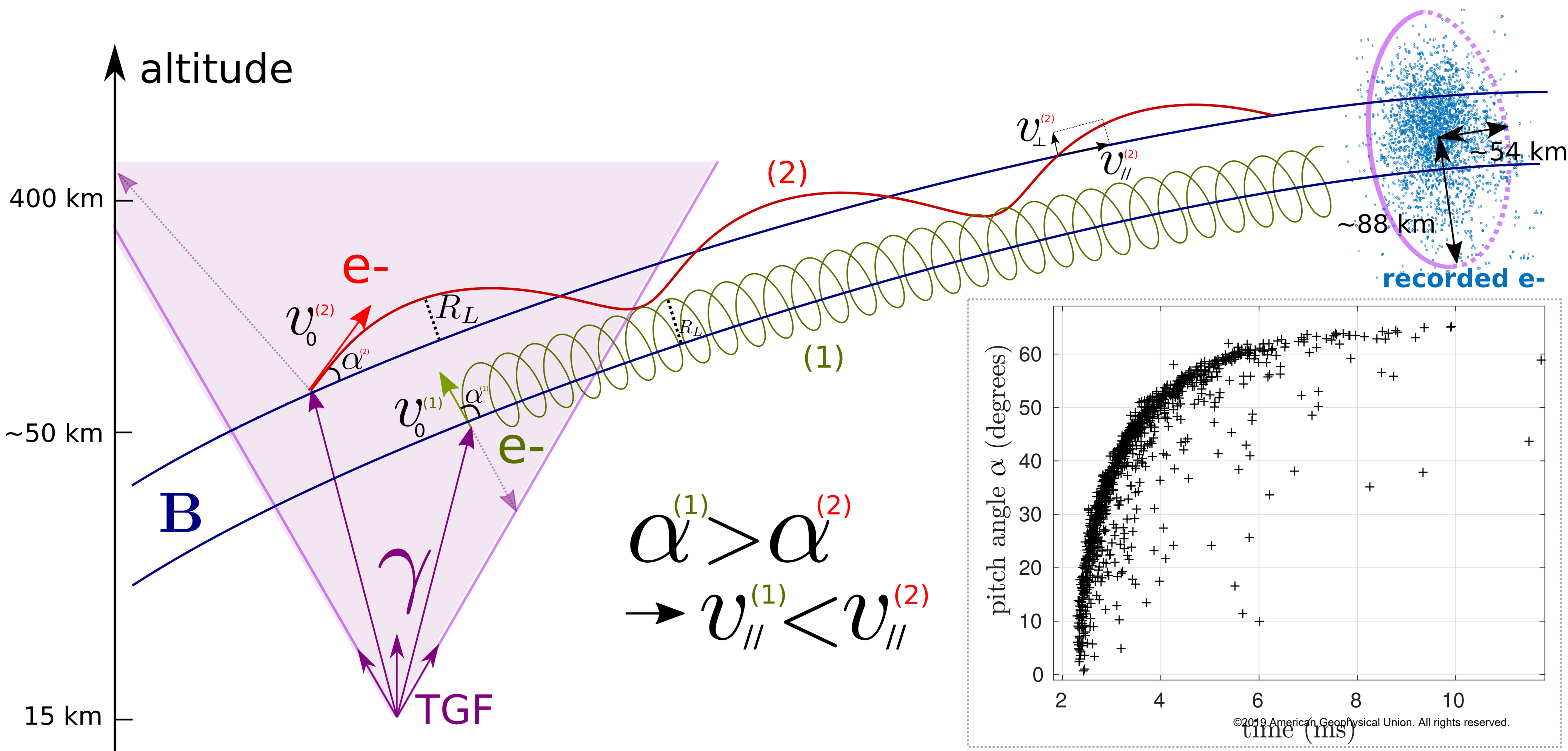
- 584 *Radio Science*, 47(6), RS6005. doi: 10.1029/2012RS005049
- 585 Lefeuvre, F., Blanc, E., & Pinçon, J. L. (2009, April). TARANIS-a Satellite Project  
586 Dedicated to the Physics of TLEs and TGFs. In *American institute of physics*  
587 *conference series* (Vol. 1118, p. 3-7). doi: 10.1063/1.3137711
- 588 Mailyan, B. G., Briggs, M. S., Cramer, E. S., Fitzpatrick, G., Roberts, O. J., Stan-  
589 bro, M., . . . Dwyer, J. R. (2016, November). The spectroscopy of individual  
590 terrestrial gamma-ray flashes: Constraining the source properties. *Journal of*  
591 *Geophysical Research (Space Physics)*, 121, 11. doi: 10.1002/2016JA022702
- 592 Marisaldi, M., Fuschino, F., Tavani, M., Dietrich, S., Price, C., Galli, M., . . . Vercel-  
593 lone, S. (2014, February). Properties of terrestrial gamma ray flashes detected  
594 by AGILE MCAL below 30 MeV. *Journal of Geophysical Research (Space*  
595 *Physics)*, 119, 1337-1355. doi: 10.1002/2013JA019301
- 596 Neubert, T., Østgaard, N., Reglero, V., Blanc, E., Chanrion, O., Oxborrow,  
597 C. A., . . . Bhanderi, D. D. V. (2019, Mar 12). The ASIM Mission on  
598 the International Space Station. *Space Science Reviews*, 215(2), 26. Re-  
599 trieved from <https://doi.org/10.1007/s11214-019-0592-z> doi:  
600 10.1007/s11214-019-0592-z
- 601 Neubert, T., Østgaard, N., Reglero, V., Chanrion, O., Heumesser, M., Dimitriadou,  
602 K., . . . Eyles, C. J. (2019). A Terrestrial Gamma-ray Flash and Ionospheric  
603 UV Emissions Powered by Lightning. *Science*. doi: 10.1126/science.aax3872
- 604 Østgaard, N., Balling, J. E., Bjørnsen, T., Brauer, P., Budtz-Jørgensen, C., Bu-  
605 jwan, W., . . . Yang, S. (2019, February). The Modular X- and Gamma-Ray  
606 Sensor (MXGS) of the ASIM Payload on the International Space Station.  
607 *Space Sci. Rev.*, 215, 23. doi: 10.1007/s11214-018-0573-7
- 608 Østgaard, N., Gjesteland, T., Stadsnes, J., Connell, P. H., & Carlson, B. (2008,  
609 February). Production altitude and time delays of the terrestrial gamma  
610 flashes: Revisiting the Burst and Transient Source Experiment spectra.  
611 *Journal of Geophysical Research (Space Physics)*, 113, A02307. doi:  
612 10.1029/2007JA012618
- 613 Østgaard, N., Neubert, T., Reglero, V., K., U., S., Y., G., G., . . . S., A.-N. (2019).  
614 First ten months of TGF observations by ASIM. *Journal of Geophysical Re-*  
615 *search (Atmospheres)*. (Accepted) doi: 10.1029/2019JD031214
- 616 Picone, J. M., Hedin, A. E., Drob, D. P., & Aikin, A. C. (2002, December).

- 617 NRLMSISE-00 empirical model of the atmosphere: Statistical comparisons  
 618 and scientific issues. *Journal of Geophysical Research (Space Physics)*, *107*,  
 619 1468. doi: 10.1029/2002JA009430
- 620 Roberts, O. J., Fitzpatrick, G., Stanbro, M., McBreen, S., Briggs, M. S., Holzworth,  
 621 R. H., ... Mailyan, B. G. (2018, May). The First Fermi-GBM Terrestrial  
 622 Gamma Ray Flash Catalog. *Journal of Geophysical Research (Space Physics)*,  
 623 *123*, 4381-4401. doi: 10.1029/2017JA024837
- 624 Rutjes, C., Sarria, D., Broberg Skeltved, A., Luque, A., Diniz, G., Østgaard, N., &  
 625 Ebert, U. (2016, November). Evaluation of Monte Carlo tools for high energy  
 626 atmospheric physics. *Geoscientific Model Development*, *9*, 3961-3974. doi:  
 627 10.5194/gmd-9-3961-2016
- 628 Sarria, D., Blelly, P.-L., Briggs, M. S., & Forme, F. (2016, May). Studying the time  
 629 histogram of a terrestrial electron beam detected from the opposite hemisphere  
 630 of its associated TGF. *Journal of Geophysical Research (Space Physics)*, *121*,  
 631 4698-4704. doi: 10.1002/2015JA021881
- 632 Sarria, D., Blelly, P.-L., & Forme, F. (2015, May). MC-PEPTITA: A Monte Carlo  
 633 model for Photon, Electron and Positron Tracking In Terrestrial Atmosphere.  
 634 Application for a terrestrial gamma ray flash. *Journal of Geophysical Research*  
 635 *(Space Physics)*, *120*, 3970-3986. doi: 10.1002/2014JA020695
- 636 Sarria, D., Lebrun, F., Blelly, P.-L., Chipaux, R., Laurent, P., Sauvaud, J.-A., ...  
 637 Lindsey-Clark, M. (2017, July). TARANIS XGRE and IDEE detection  
 638 capability of terrestrial gamma-ray flashes and associated electron beams.  
 639 *Geoscientific Instrumentation, Methods and Data Systems*, *6*, 239-256. doi:  
 640 10.5194/gi-6-239-2017
- 641 Smith, D. M., Grefenstette, B. W., Splitt, M., Lazarus, S. M., Rassoul, H. K., Cole-  
 642 man, L. M., ... Takahashi, Y. (2006, December). The Anomalous Terrestrial  
 643 Gamma-ray Flash of 17 January 2004. *AGU Fall Meeting Abstracts*, AE31A-  
 644 1040.
- 645 Smith, D. M., Lopez, L. I., Lin, R. P., & Barrington-Leigh, C. P. (2005, February).  
 646 Terrestrial Gamma-Ray Flashes Observed up to 20 MeV. *Science*, *307*, 1085-  
 647 1088. doi: 10.1126/science.1107466
- 648 Stanbro, M., Briggs, M., Roberts, O., Cramer, E., Dwyer, J., Holzworth, R., ...  
 649 Xiong, S. (2019). A fermi gamma-ray burst monitor event observed as

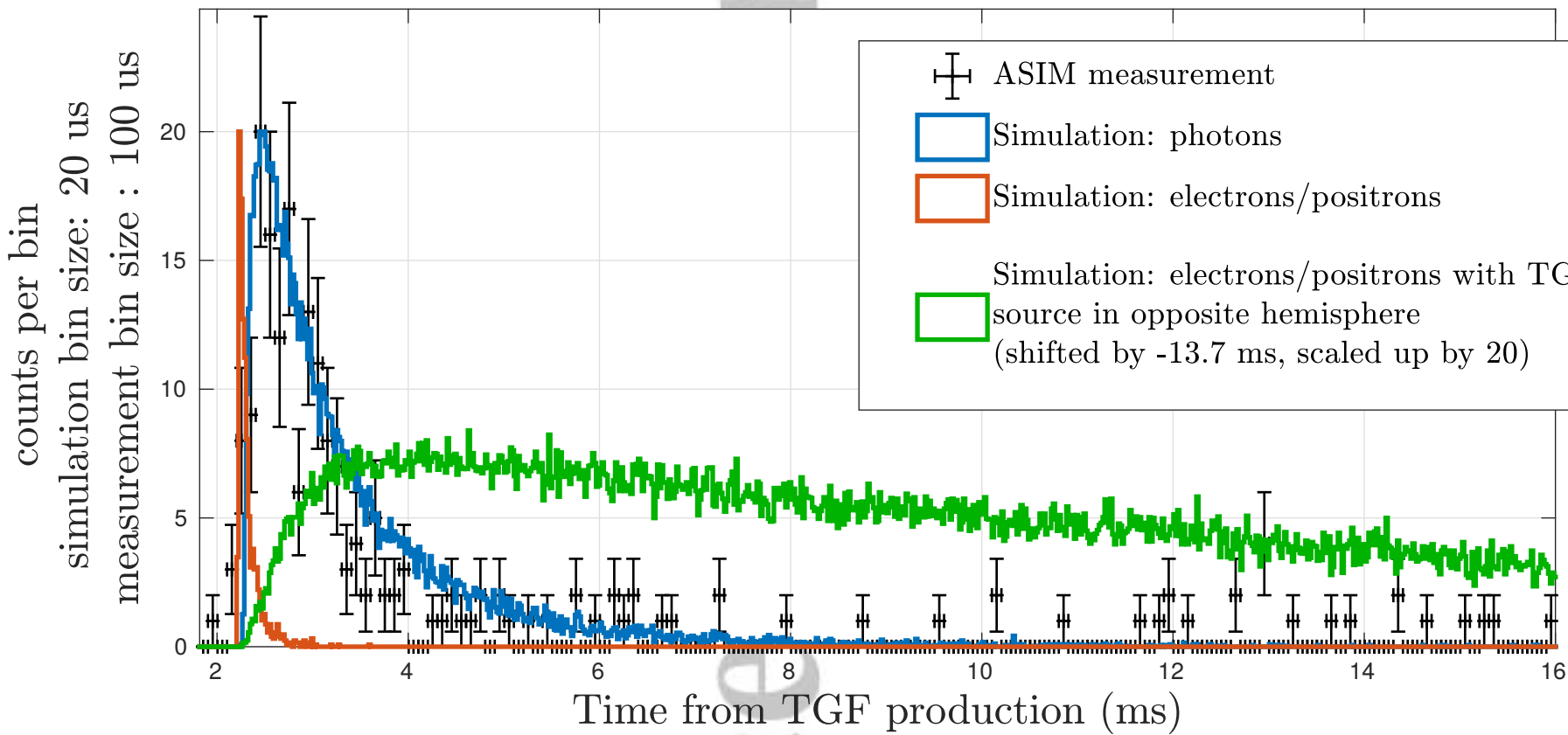
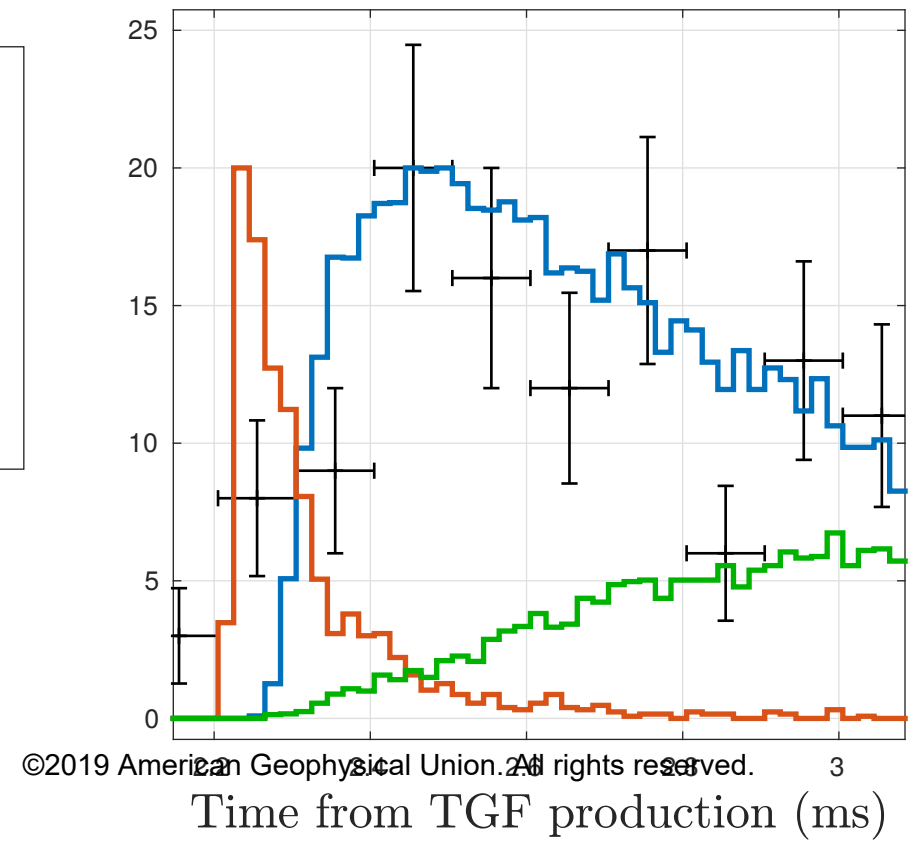
650 a terrestrial gamma-ray flash and terrestrial electron beam. *Journal of*  
651 *Geophysical Research: Space Physics*, 0(ja). Retrieved from [https://](https://agupubs.onlinelibrary.wiley.com/doi/abs/10.1029/2019JA026749)  
652 [agupubs.onlinelibrary.wiley.com/doi/abs/10.1029/2019JA026749](https://agupubs.onlinelibrary.wiley.com/doi/abs/10.1029/2019JA026749) doi:  
653 10.1029/2019JA026749  
654 Thébault, E., Finlay, C. C., Beggan, C. D., Alken, P., Aubert, J., Barrois, O.,  
655 ... Zvereva, T. (2015, May). International Geomagnetic Reference  
656 Field: the 12th generation. *Earth, Planets, and Space*, 67, 79. doi:  
657 10.1186/s40623-015-0228-9  
658 Ursi, A., Guidorzi, C., Marisaldi, M., Sarria, D., & Frontera, F. (2017, April). Ter-  
659 restrial gamma-ray flashes in the BeppoSAX data archive. *Journal of Atmo-*  
660 *spheric and Solar-Terrestrial Physics*, 156, 50-56. doi: 10.1016/j.jastp.2017.02  
661 .014

Figure 1.

Accepted Article



Accepted Article

**a.****b.**

Accepted Article

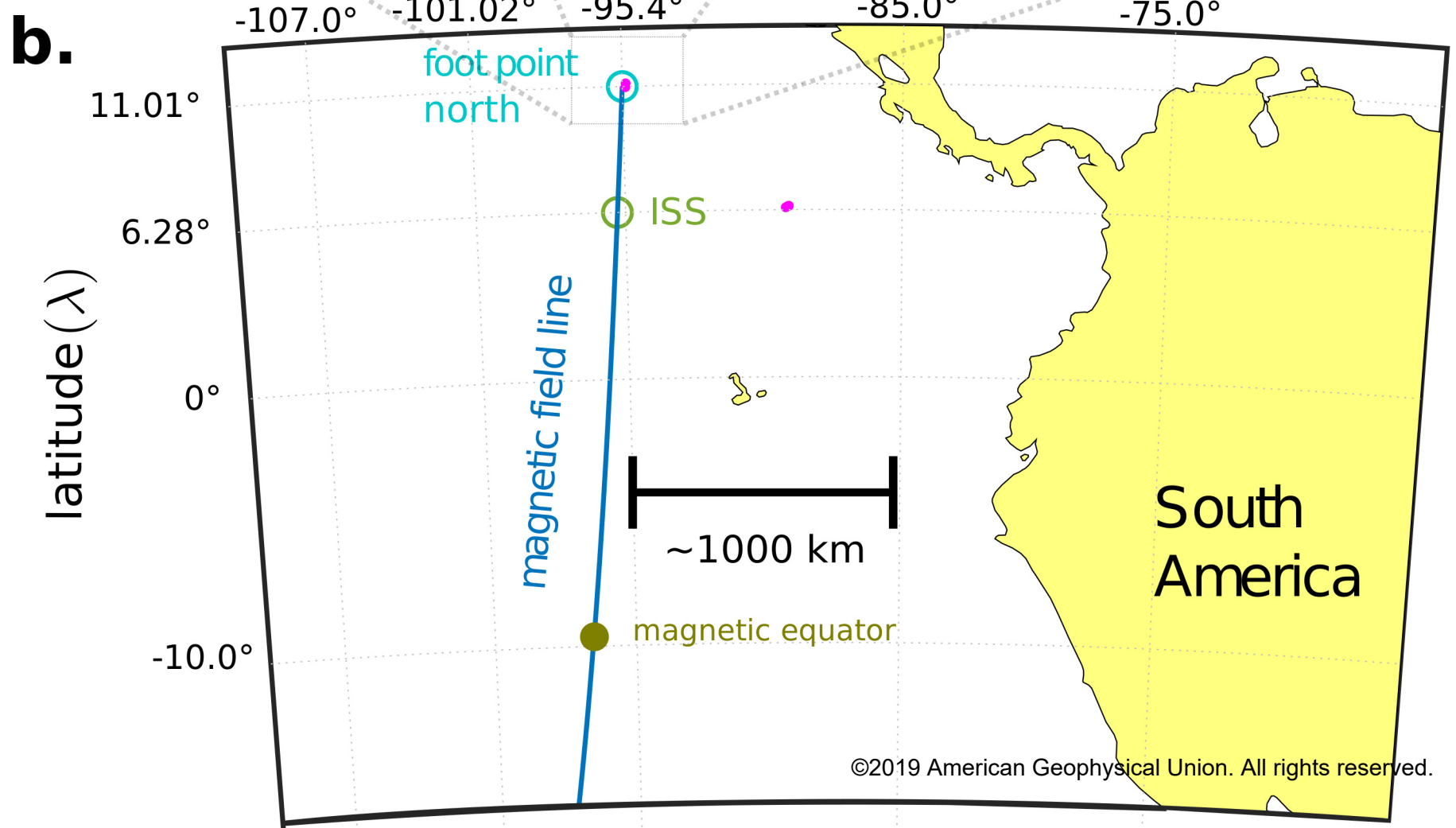
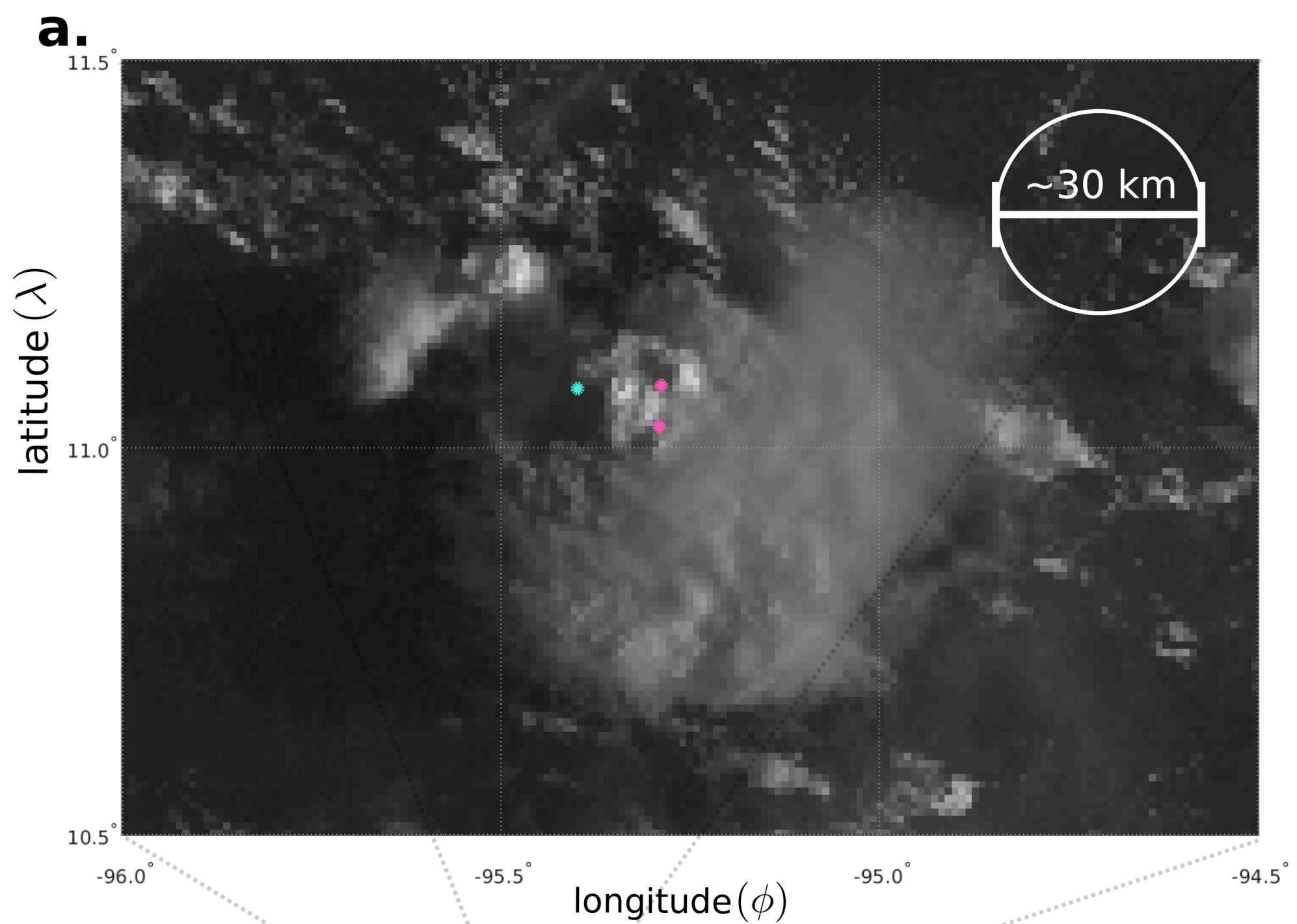
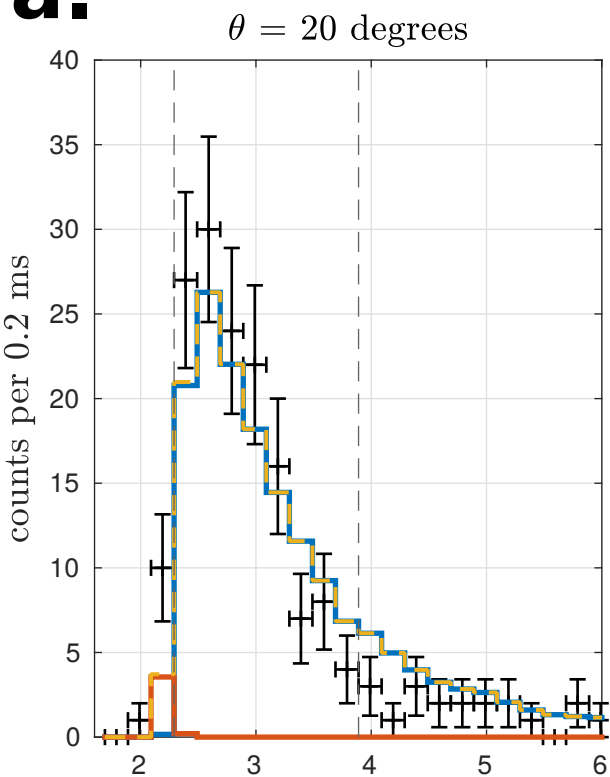
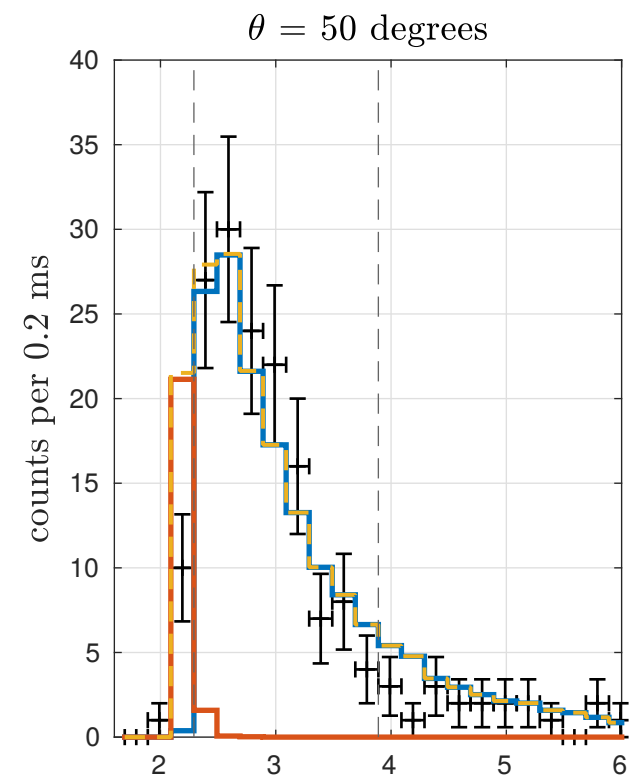
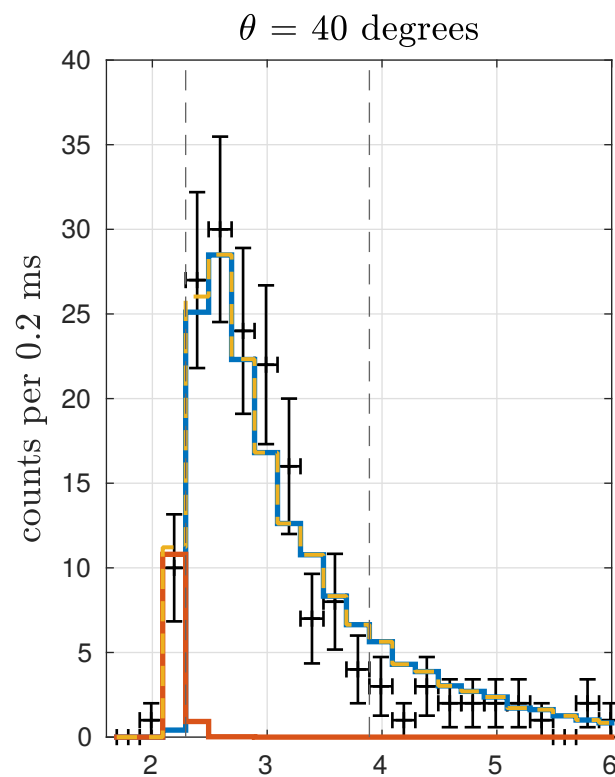
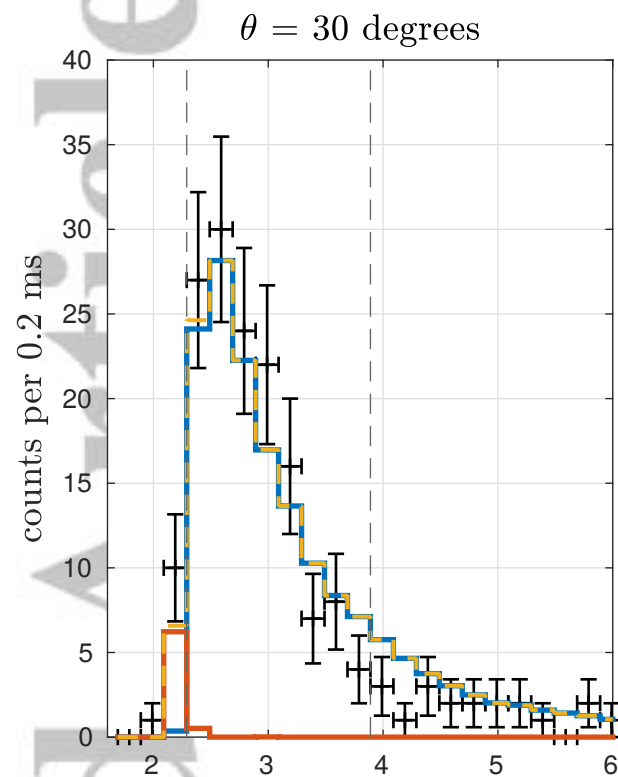


Figure 4.

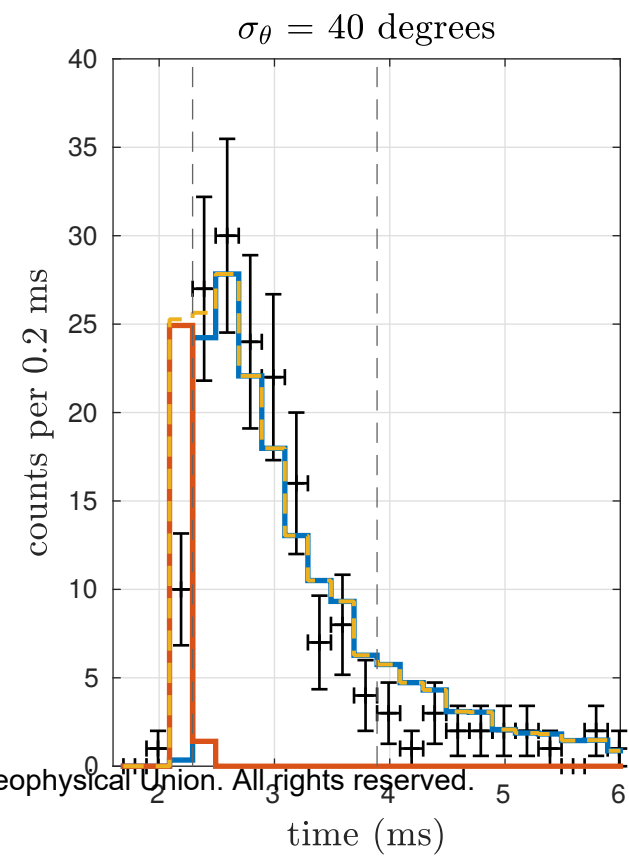
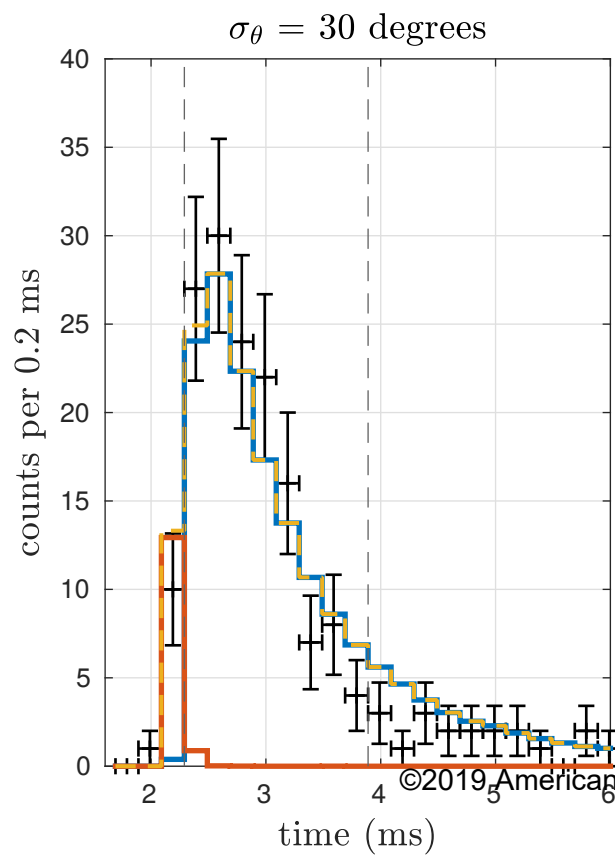
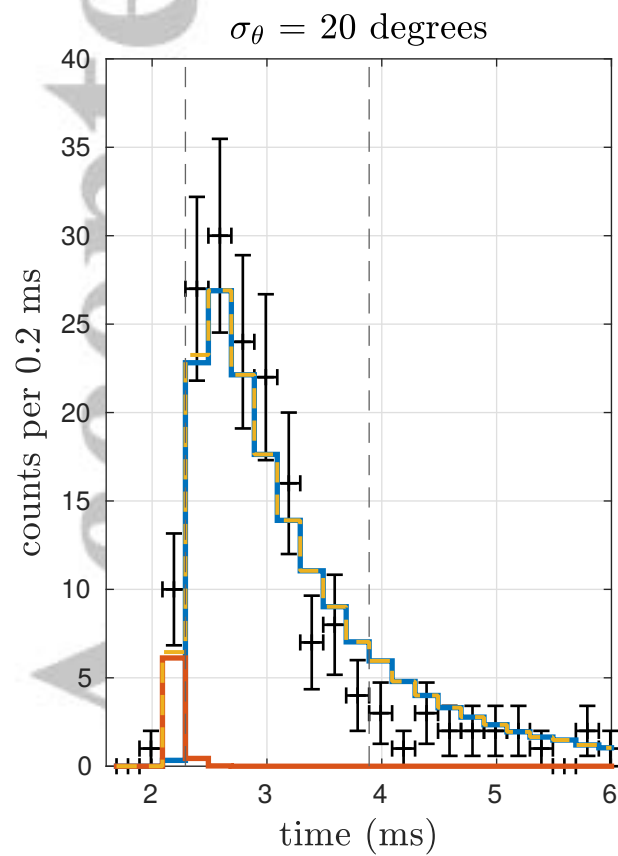
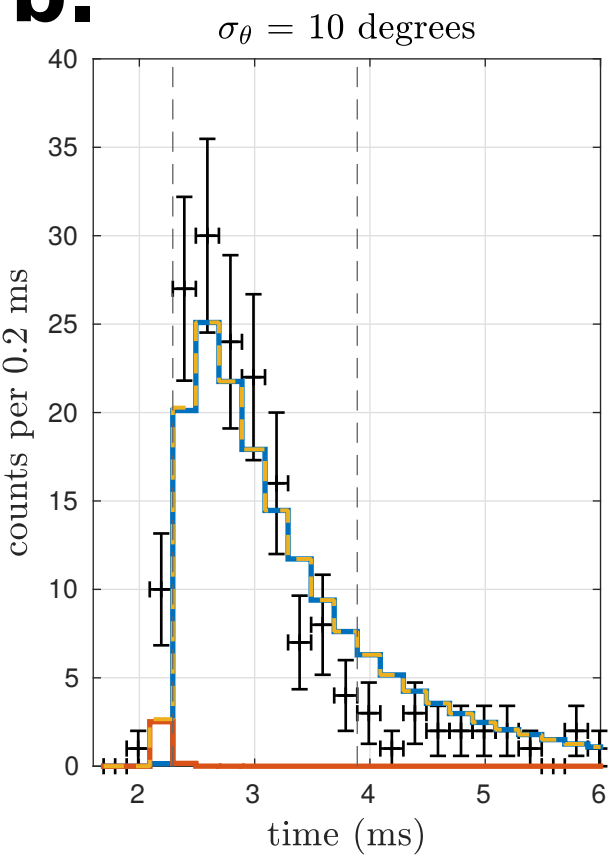
Accepted Article

**a.**

## Angular distribution: isotropic within cone



ASIM Measurement  
 simulation: electrons/positrons  
 simulation: photons  
 simulation: sum

**b.**

## Angular distribution: Gaussian

Figure 5.

Accepted Article

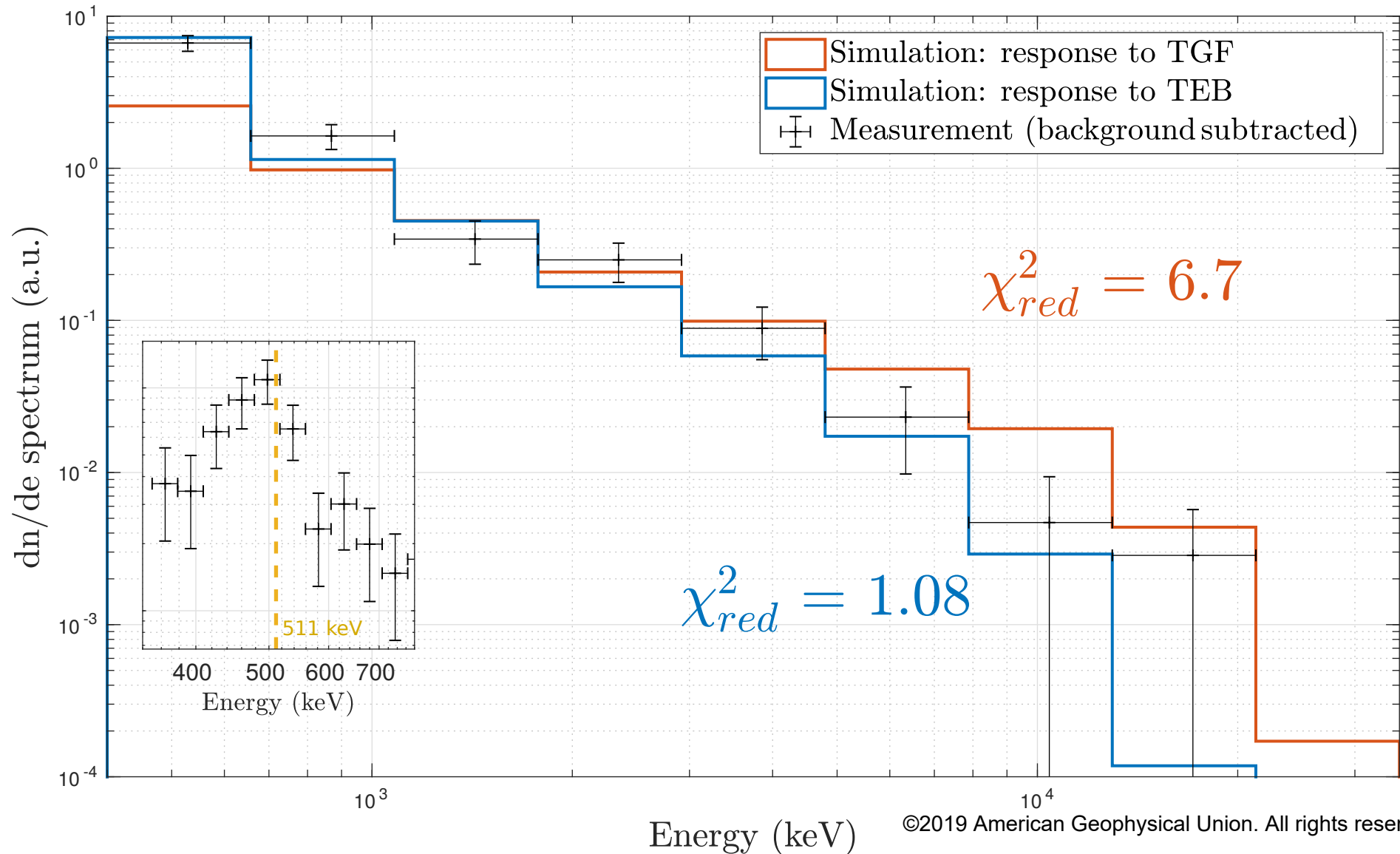
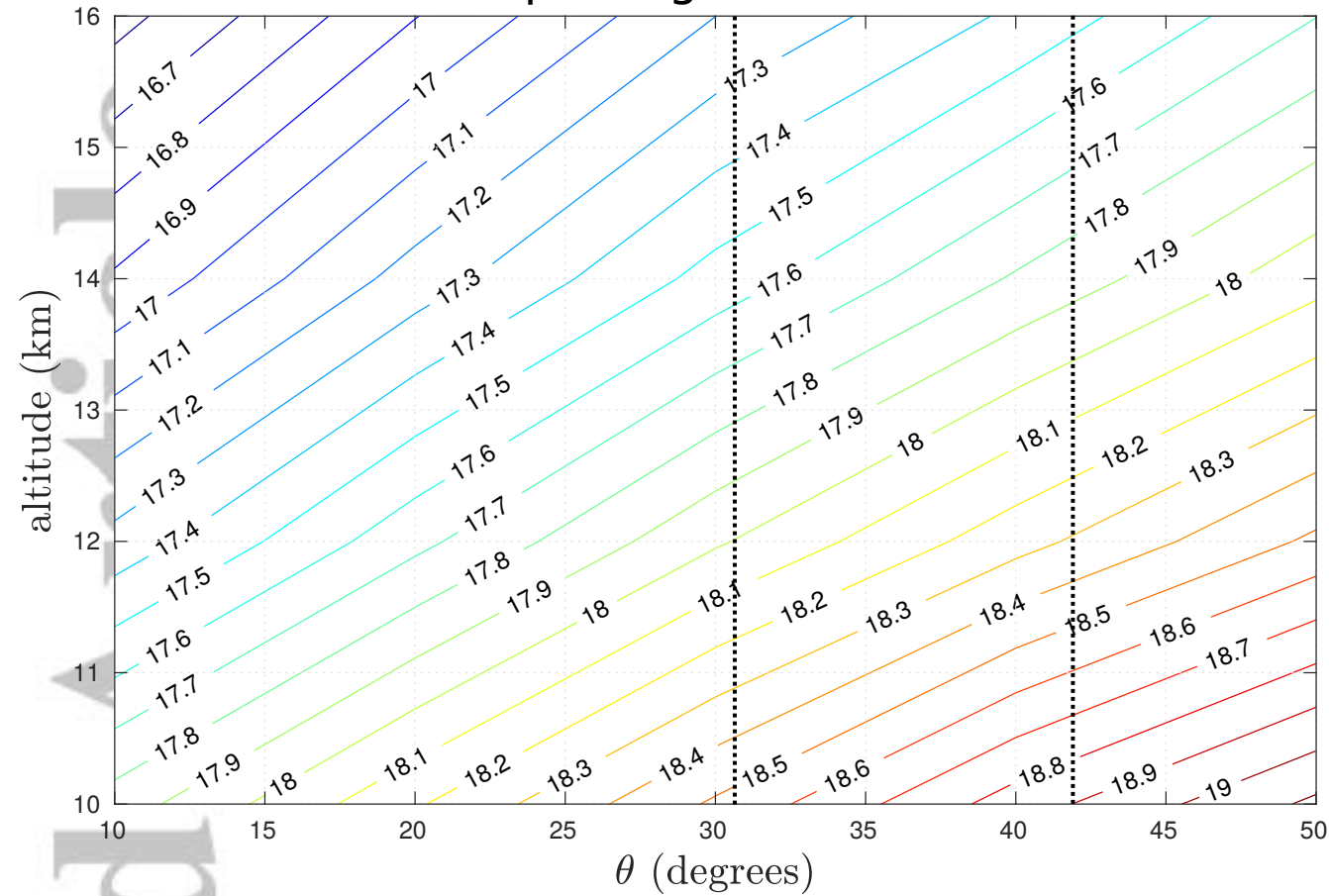


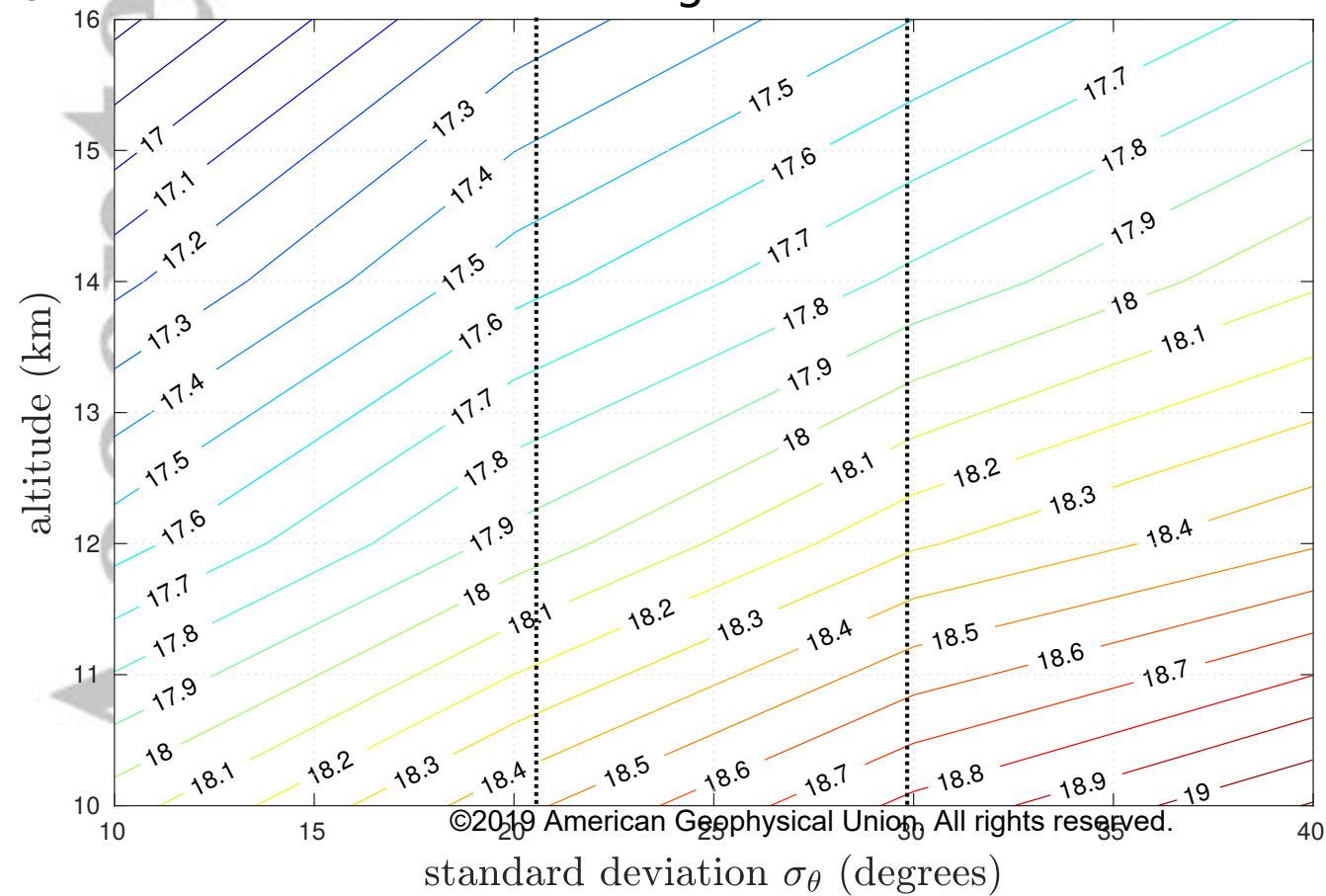
Figure 6.

Accepted Article

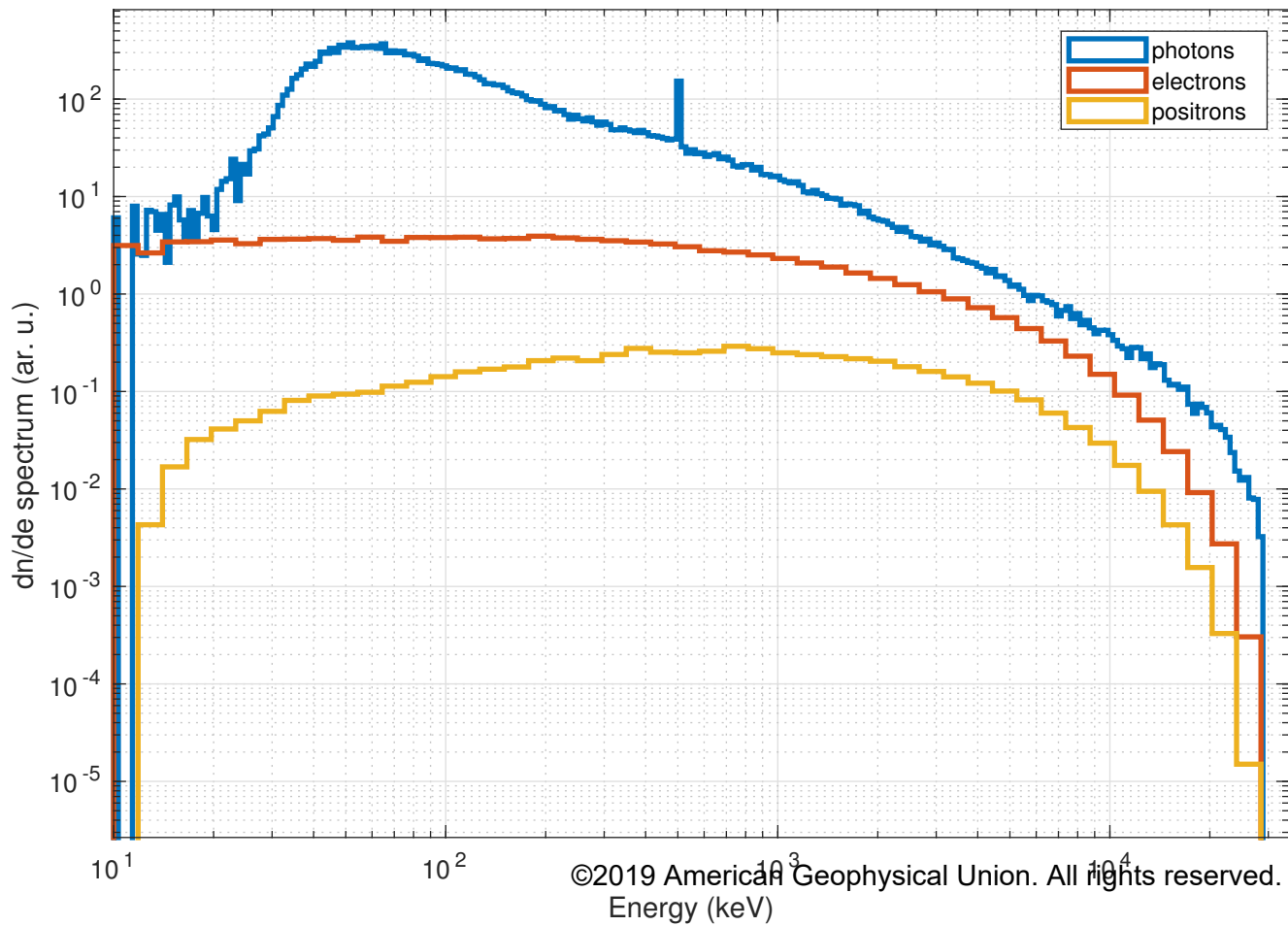
# a. Isotropic angular distribution



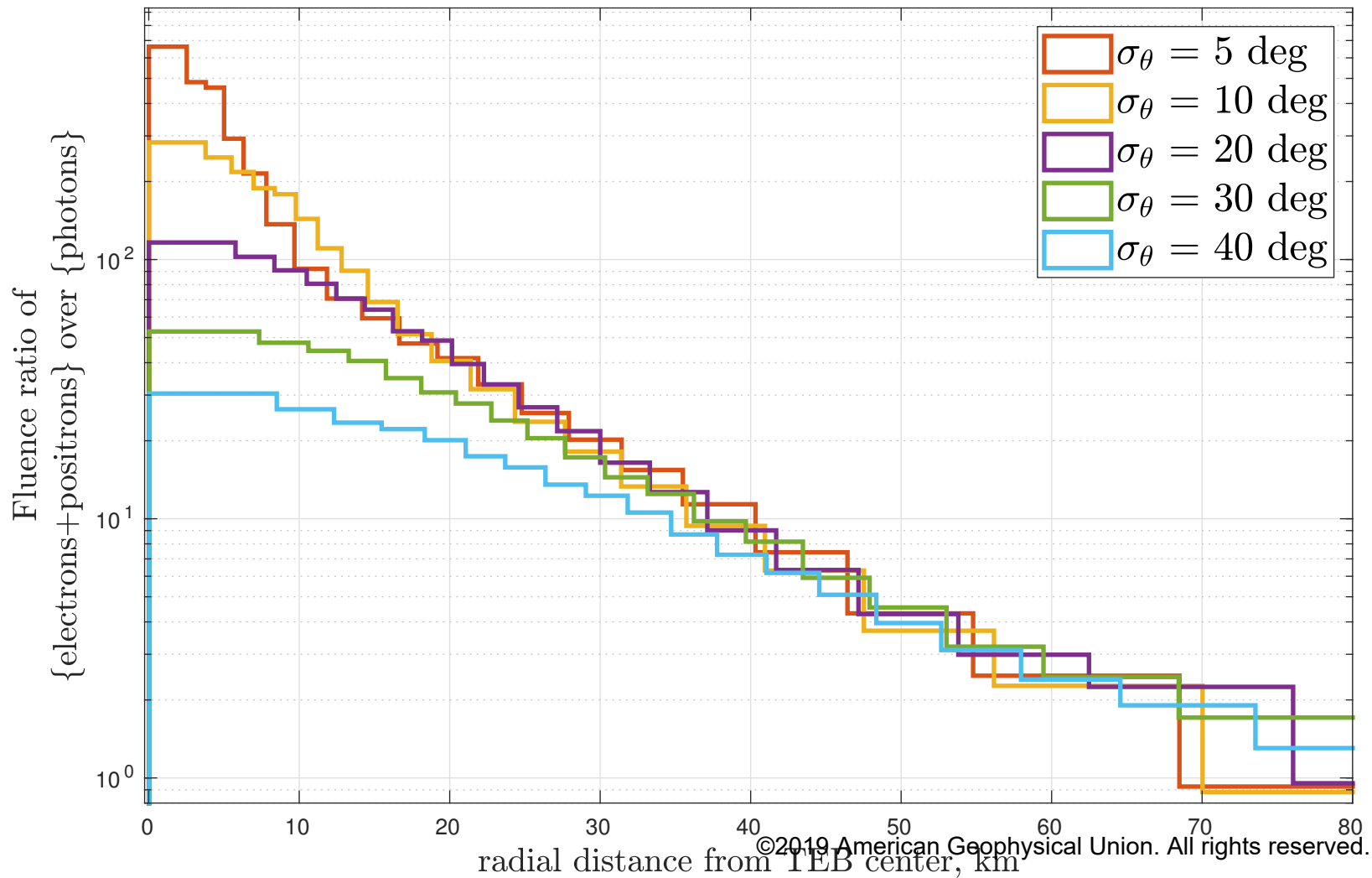
# b. Gaussian angular distribution



Accepted Article

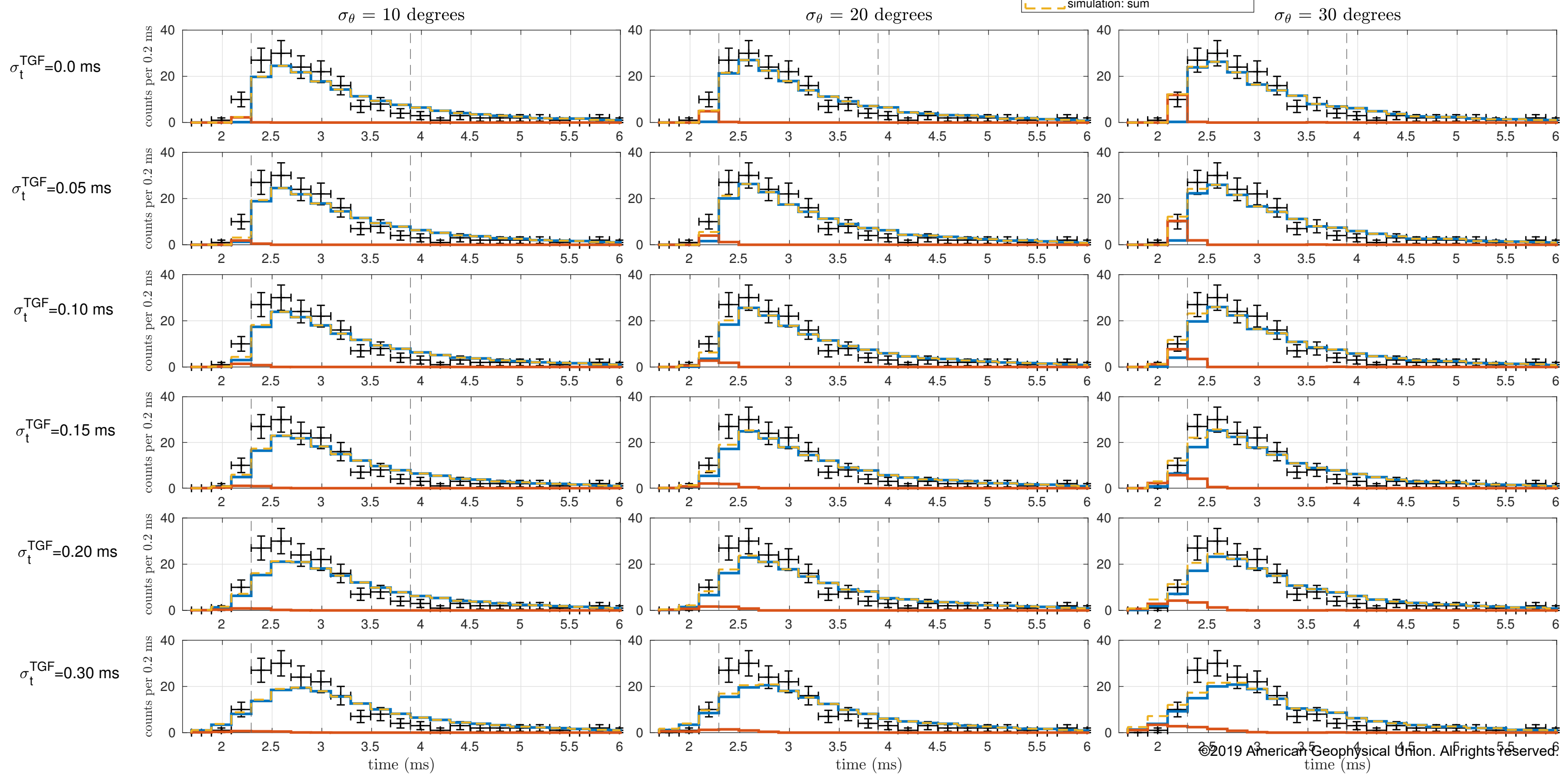
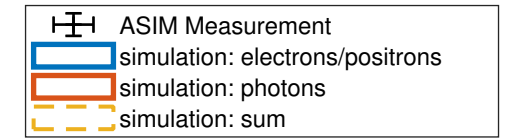


Accepted Article



Accepted Article

# Gaussian angular distribution



Accepted Article

